Article

Discovery Medicine 2026; 38(208): 1458–1477
https://doi.org/10.24976/Discov.Med.202638208.114

Untargeted Metabolomic Profiling Reveals Bone Tissue Metabolic Alterations Associated With Acute Bone Loss Following Fracture and Unloading

Bingchao Wu[1], Zongrui Wang[1], Mingjian Bei[1], Xinbao Wu[1,*]

[1]Department of Orthopaedic Trauma, Beijing Jishuitan Hospital, Capital Medical University, 100035 Beijing, China
*Correspondence: wuxinbao_jst@126.com (Xinbao Wu)
Submitted: 18 March 2026 Revised: 30 March 2026 Accepted: 29 April 2026 Published: 20 May 2026

Background: Fracture healing is strongly influenced by mechanical loading conditions, whereas hindlimb unloading induces bone loss and may further compromise skeletal repair. However, the metabolic remodeling of bone tissue under fracture, unloading, and their combination remains insufficiently characterized. This study aimed to investigate metabolic alterations in mouse bone tissue under fracture (Fx), tail-suspension hindlimb unloading group (HU), and fracture combined with tail-suspension hindlimb unloading group (Fx + HU) using untargeted metabolomics.

Methods: Male mice were randomly assigned to four groups: sham control (Sham), Fx, HU, and Fx + HU. Mechanical unloading was induced using a tail-suspension hindlimb unloading model, and fracture was established using a standardized murine fracture procedure. After 3 weeks of intervention, proximal tibial bone tissues were collected for micro-computed tomography (micro-CT) and untargeted metabolomics analysis. Multivariate statistical analyses, including principal component analysis (PCA), partial least squares discriminant analysis (PLS-DA), and orthogonal PLS-DA (OPLS-DA), were performed to identify metabolic differences among groups. Differential metabolites and enriched pathways were further analyzed.

Results: Micro-CT analysis showed significant deterioration of trabecular bone mass and microarchitecture in the Fx, HU, and Fx + HU groups compared with the Sham group (all $p < 0.001$), with the Fx + HU group showing the most pronounced impairment. Untargeted metabolomics demonstrated robust analytical reproducibility in both positive and negative ion modes. PCA and supervised multivariate analyses showed clear separation among the four groups, and the Fx + HU group exhibited the greatest metabolic divergence from the others. Differential metabolite screening and pathway enrichment analysis revealed marked alterations in metabolic pathways associated with amino acid metabolism, lipid metabolism, energy metabolism, and oxidative stress-related processes.

Conclusions: Fracture and hindlimb unloading each induced substantial metabolic remodeling in mouse bone tissue, while their combination produced more profound and distinct metabolic perturbations. These findings suggest that mechanical unloading may aggravate bone metabolic dysregulation after fracture and provide exploratory metabolomic evidence for understanding skeletal deterioration under combined injury and unloading conditions.

Keywords: fracture; hindlimb unloading; untargeted metabolomics; bone metabolism; micro-computed tomography; bone loss

Introduction

Fracture is a prevalent skeletal injury, traditionally investigated as a localized structural phenomenon with a primary focus on local healing mechanisms [1,2]. However, mounting evidence indicates that a fracture triggers widespread systemic alterations in bone metabolism, often culminating in acute post-fracture bone loss at remote, non-injured skeletal sites [3,4]. This underscores that fracture represents a significant biological stress capable of initiating a systemic skeletal remodeling response [5,6]. Concurrently, mechanical unloading—a condition inherent to post-fracture immobilization—is a well-established, independent factor driving rapid bone loss through its adverse effects on bone formation and resorption [7].

While fracture and unloading are frequently co-present in clinical settings, their combined impacts on bone metabolism remain poorly understood. One possible explanation may be the neglect of synergistic or non-additive metabolic disturbances when both injuries exist simultaneously. Bone homeostasis is governed by complex metabolic networks involving processes such as energy metabolism, substance transport, and inflammatory signaling [8]. Untargeted metabolomics offers a powerful, unbiased platform to capture such complex systemic metabolic changes.

In this study, we integrated high-resolution micro-computed tomography (micro-CT) with untargeted metabolomics to systematically investigate bone microarchitecture and metabolic alterations in a mouse model of tibial fracture, hindlimb unloading, and their combination.

Our central hypothesis is that fracture and mechanical unloading induce distinct but interdependent metabolic reprogramming in bone tissue, and that their combination results in a unique metabolic and structural disturbance that surpasses the additive effects of either condition alone. Specifically, we sought to characterize the bone tissue metabolic signature associated with each intervention, determine whether their combined effect induces a unique metabolic profile, and identify key metabolic pathways and metabolites associated with compromised bone microarchitecture. Our study aims to provide a metabolic framework for understanding the compounded risk of bone loss in clinical scenarios involving skeletal injury and immobilization, potentially informing the development of novel therapeutic or preventive strategies.

Materials and Methods

Animals and Experimental Design

Forty male C57BL/6N mice, aged 8 weeks and weighing 23–25 g at baseline, were obtained from Beijing Sibaifu Experimental Animal Technology Co., Ltd. All animals were housed under specific pathogen-free conditions and acclimated for 1 week before experimental procedures. The environment is maintained under constant temperature and humidity, with a fixed 12-hour light/dark cycle, and free access to food and drinking water. The study protocol was reviewed and approved by the Institutional Animal Care and Use Committee of Beijing Jishuitan Hospital, Capital Medical University (approval No. [2025-02-05]). All procedures were performed in accordance with the Guide for the Care and Use of Laboratory Animals and relevant institutional guidelines.

After acclimation, mice were randomly assigned into four experimental groups (n = 10 per group) based on fracture induction and/or mechanical unloading: the sham group (Sham), which underwent anesthesia and handling without fracture or unloading; the Fx, in which a standardized fracture model was established; the HU, in which mechanical unloading was induced by tail suspension; and the Fx + HU, in which both fracture induction and hindlimb unloading were performed.

Mechanical unloading was achieved using a tail-suspension model adapted from the classical protocol described by Morey-Holton and Globus [9], which effectively simulates weight-bearing deprivation and has been widely used to study unloading-induced bone loss [10]. The fracture model was performed in the mode of fracture healing and bone reconstruction after fracture.

The total experimental duration was 4 weeks. The first week served as the acclimation period. Beginning in the second week, fracture induction and/or hindlimb unloading were initiated according to group assignment. Following model establishment, the respective interventions were maintained for 3 weeks. At the end of the third week after model induction, all mice were euthanized by cervical dislocation performed by trained personnel. Death was confirmed by the absence of heartbeat and respiratory movement. All procedures were conducted in accordance with institutional guidelines for animal care and were approved by the relevant ethics committee. Bone tissues were subsequently harvested for micro-CT analysis and metabolomic profiling.

Fracture Model Establishment

Mice in the Fx and Fx + HU groups were anesthetized via intraperitoneal injection of a ketamine/xylazine mixture (e.g., 100 mg/kg ketamine and 10 mg/kg xylazine) and placed in the supine position. The right hindlimb was routinely shaved and disinfected. A standardized closed tibial fracture model was then established using a controlled mechanical impact, as previously described in murine fracture studies [11–13]. Briefly, following fracture induction, a 26-gauge stainless steel pin was inserted through the proximal tibia into the medullary cavity to achieve intramedullary fixation and maintain fracture stability.

Post-operative analgesia (e.g., subcutaneous carprofen, 5 mg/kg) was administered for 3 days. Mice were monitored daily for signs of infection, distress, or weight loss exceeding 20% of baseline. Postoperative radiographic imaging was performed immediately after surgery to verify fracture location and confirm correct positioning of the intramedullary fixation, thereby ensuring successful and reproducible model establishment.

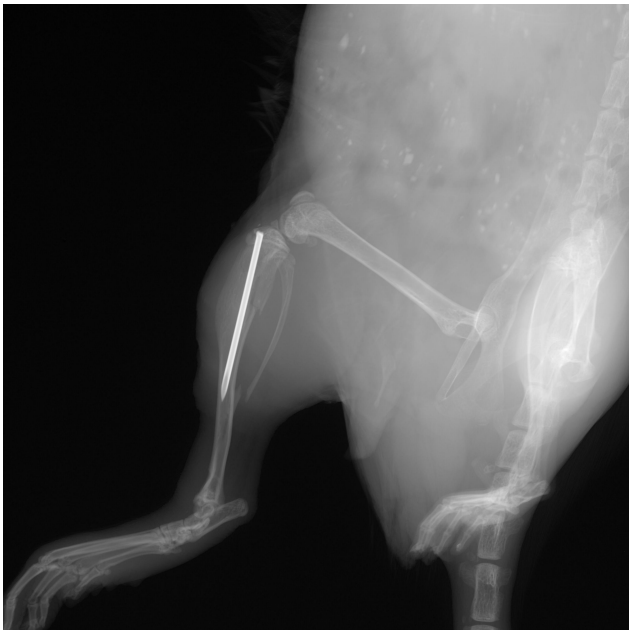

Fig. 1. Representative X-ray image of the murine tibial fracture model (immediately after surgery), showing the fracture location and fixation status.

Although mice in the Sham and HU groups did not undergo fracture surgery, they received identical anesthesia and handling procedures during the experimental process when other groups (such as the Fx and Fx + HU groups) required anesthesia and surgery. This was done to control experimental variables, ensuring that environmental factors—such as anesthetic stress and handling duration—had as consistent an impact as possible across all groups, independent of fracture intervention. This design enables the study to distinguish and compare the independent effects of fracture and mechanical unloading, as well as their combined effects on bone tissue (Fig. 1).

Hindlimb Unloading Protocol

Mice in the HU and Fx + HU groups were subjected to a classical tail suspension–based hindlimb unloading model to simulate reduced mechanical loading, as previously described [14–16]. Briefly, prior to suspension, the proximal portion of the tail was cleaned and thoroughly dried. Medical adhesive tape was applied longitudinally along the tail and connected to a suspension apparatus attached to a crossbar or sliding rail at the top of the cage, allowing free anterior–posterior movement within the cage. The taped region was further secured with a light, porous bandage wrap to distribute tension and prevent skin injury.

The suspension height was adjusted to maintain a head-down tilt of approximately 30 °C, ensuring complete elevation of the hindlimbs from the cage floor and elimination of weight bearing, while the forelimbs remained in normal contact with the floor to allow unrestricted locomotion, feeding, and drinking. This configuration effectively eliminated mechanical loading from the hindlimbs and established a stable and reproducible unloading condition.

Throughout the unloading period, mice were housed under standard laboratory conditions. The height of food and water bottles was adjusted to minimize feeding difficulty. General health status, including activity level, food and water intake, and body weight, was monitored daily. Particular attention was paid to tail skin integrity and circulation, and the suspension apparatus was regularly inspected and adjusted to prevent tail ischemia, skin injury, or unintended hindlimb contact with the cage floor.

Micro-CT Analysis

Mouse tibiae were scanned and three-dimensionally reconstructed using a high-resolution micro-CT system (Skyscan 1172; Bruker microCT, N.V., Aartselaar, Belgium). Scanning was performed with the following parameters: X-ray tube voltage of 50 kV, tube current of 200 µA, a 0.5 mm aluminum filter, isotropic voxel size of 9 µm, rotation angle of 180°, rotation step of 0.4°, and exposure time of 300 ms. During scanning, specimens were securely mounted to minimize motion artifacts.

Raw projection images were reconstructed using NRecon software (version 1.7.4.2, Bruker microCT, Kontich, Belgium), with identical settings for beam hardening correction and ring artifact reduction applied to all samples to ensure consistency. Quantitative analyses were subsequently conducted using CTAn software (Bruker microCT).

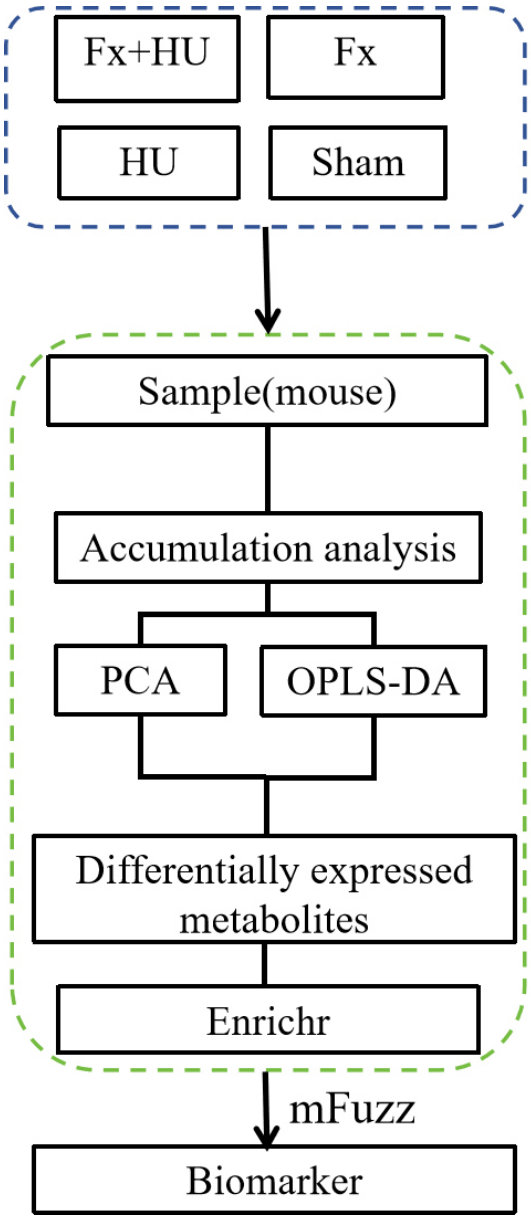

Fig. 2. Workflow of the untargeted metabolomics analysis. Forty mice were initially randomized into four groups (n = 10 per group). Abbreviations: Sham, sham control; Fx, fracture; HU, tail-suspension hindlimb unloading group; Fx + HU, fracture combined with tail-suspension hindlimb unloading group; PCA, principal component analysis; OPLS-DA, orthogonal partial least squares discriminant analysis.

On the reconstructed three-dimensional images, a standardized region of interest (ROI) was defined within the trabecular bone compartment immediately distal to the tibial plateau. The location and volume of the ROI were kept

identical across all specimens. Regions containing fracture lines or callus formation were deliberately excluded to ensure that only trabecular bone tissue was analyzed. Trabecular bone was segmented using a uniform global threshold, and bone mineral density (BMD) was calculated. In addition, trabecular microarchitectural parameters, including bone volume fraction (BV/TV), trabecular thickness (Tb.Th), trabecular number (Tb.N), and trabecular separation (Tb.Sp), were quantified to comprehensively assess changes in bone mass and microstructure under different experimental conditions.

All micro-CT image acquisition and analyses were performed by the same investigator under blinded conditions (unaware of group assignments) to minimize measurement bias. Trabecular bone was segmented using a uniform global threshold, which was visually verified and applied consistently to all samples, enabling separation of bone from background voxels based on the grayscale histogram.

Untargeted Metabolomics Analysis

Untargeted metabolomics was performed to systematically characterize metabolic profiles of mouse tibial bone tissues under different experimental conditions, including the Fx + HU, Fx, HU, and Sham (Fig. 2). Proximal tibial bone tissues were collected as analytical samples. After careful removal of surrounding soft tissues, samples were rapidly processed, snap-frozen in liquid nitrogen, and stored at –80 °C until analysis. All samples were extracted, analyzed, and acquired under identical experimental conditions to minimize technical variation and analytical bias.

Sample Collection and Preparation

At the end of the third week following fracture induction and/or hindlimb unloading, all mice were euthanized at the same predefined time point to ensure comparability among groups. Immediately after euthanasia, the proximal tibial region was dissected, and bone tissue samples were collected for subsequent untargeted metabolomics analysis [17,18].

Both tibiae were then rapidly dissected and carefully cleared of surrounding soft tissues. For each mouse, the right tibia was retained for downstream analyses and longitudinally divided into two portions. One portion was fixed immediately for subsequent micro-CT scanning and three-dimensional reconstruction, while the other portion was snap-frozen in liquid nitrogen and stored at –80 °C. From the frozen samples, trabecular bone from the proximal tibial region (tibial plateau) was harvested for untargeted metabolomics analysis. Approximately 30 mg of bone tissue was weighed and homogenized in a cold methanol/water mixture (e.g., 80:20, v/v) at a ratio of 10:1 (solvent: tissue, v/m) for metabolite extraction. As this region is highly sensitive to changes in mechanical loading and fracture-induced bone remodeling [19].

Throughout all sampling and processing procedures, handling time was minimized to reduce postmortem metabolic alterations and preserve the *in vivo* metabolic state of the tissues.

Liquid Chromatography-Mass Spectrometry (LC-MS) Data Acquisition and Quality Control

Chromatographic separation was performed on a C18 column (e.g., Waters ACQUITY UPLC BEH C18, 2.1 × 100 mm, 1.7 µm) maintained at 40 °C, with a flow rate of 0.3 mL/min. The mobile phase consisted of (A) water with 0.1% formic acid and (B) acetonitrile with 0.1% formic acid. Mass spectrometry analysis was conducted in both positive and negative electrospray ionization (ESI) modes with the following source parameters: capillary voltage, 3.0 kV; source temperature, 120 °C; desolvation gas flow, 600 L/h. To monitor instrument stability and reproducibility, a pooled quality control (QC) sample, created by mixing equal aliquots from all experimental samples, was injected at regular intervals (every 10th injection) throughout the analytical sequence.

To explore global metabolic variations and characterize metabolic differences among experimental groups, multivariate statistical analyses were performed based on the identified metabolites. All analyses were conducted separately in positive and negative ion modes. Principal component analysis (PCA) was performed using the FactoMineR R package (v2.12) as an unsupervised method to assess overall metabolic variation, sample distribution, and intrinsic clustering patterns among the Sham, Fx, HU, and Fx + HU groups.

Partial least squares discriminant analysis (PLS-DA) was conducted using the ropls R package (v1.38.0) as a supervised multivariate approach to further evaluate group discrimination and to identify metabolites contributing to intergroup separation [20]. Model performance and robustness were assessed using the cumulative explained variance of response variables (R^2Y) and the predictive ability parameter (Q^2) obtained through 7-fold cross-validation. Models were considered robust and not overfitted when they demonstrated a satisfactory balance of high fit (R^2Y) and high predictive ability ($Q^2 > 0.5$), and when permutation tests (with 200 iterations) confirmed that the original model's Q^2 and R^2Y values were significantly higher than those of the permuted models. A Q^2 value >0.5 was considered indicative of good model predictability [21].

Data Preprocessing

To identify differential metabolites between experimental groups, pairwise comparisons were performed among the Fx + HU, Fx, HU, and Sham groups using univariate statistical analysis. Analyses were conducted separately in positive and negative ion modes.

Differential metabolites were defined based on combined multivariate and univariate criteria: variable impor-

tance in projection (VIP) >1 derived from orthogonal partial least squares discriminant analysis (OPLS-DA) models, absolute $\log_2$ fold change ($|\log_2 FC|$) >1, and $p < 0.05$ [22–24]. Metabolites meeting all three criteria were considered significantly differentially expressed metabolites (DEMs).

Multivariate Analysis

To elucidate the biological pathways involved in the observed metabolic alterations, Kyoto Encyclopedia of Genes and Genomes (KEGG) pathway enrichment analysis was performed for the identified differential metabolites. Enrichment analysis was conducted using the KEGG Metabolite Enrichment R package (v0.1.0), based on curated KEGG pathway annotations [25,26].

Metabolites meeting the criteria of VIP >1 (from OPLS-DA models) and $p < 0.05$ were included in the enrichment analysis. Pathways with a p-value < 0.05 were considered significantly enriched, consistent with commonly adopted metabolomics enrichment strategies [27].

Differential Metabolite Screening

To identify metabolites exhibiting coordinated expression patterns across different experimental conditions, fuzzy c-means clustering analysis was performed using the Mfuzz algorithm, which is particularly suitable for noisy, high-dimensional metabolomics data and allows gradual transitions in expression patterns [28].

Clustering analyses were conducted separately in positive and negative ion modes using the ClusterGVis R package (v0.1.4). To characterize progressive metabolic alterations associated with combined intervention, two predefined stepwise progression schemes were applied:

(i) Sham → Fx → Fx + HU, representing the incremental effect of hindlimb unloading under fracture conditions;

(ii) Sham → HU → Fx + HU, representing the incremental effect of fracture under unloading conditions.

Clusters displaying monotonically increasing or decreasing expression trends along either progression scheme were defined as key clusters and selected for subsequent analyses [29].

To identify metabolites closely associated with progressive metabolic alterations induced by the combined intervention, key metabolites were screened by integrating results from multivariate discrimination and clustering analyses. Specifically, metabolites meeting the criteria of VIP >1 (derived from OPLS-DA models) and $p < 0.05$ were intersected with metabolites belonging to key Mfuzz clusters identified under the predefined stepwise progression schemes.

For each stepwise comparison framework, metabolites that were consistently identified as differential in the corresponding pairwise comparisons and simultaneously exhibited monotonic expression trends within key clusters were defined as key metabolites. Intersection analyses were performed using the ggvenn R package (v0.1.19), and results were visualized using the UpSetR R package (v1.4.0) [29].

Table 1. Baseline and pre-sacrifice body weight of mice in each group.

Group	Baseline weight (g)	Pre-sacrifice weight (g)
Sham	23.61 ± 0.99	26.73 ± 1.80[a]
HU	23.87 ± 0.64	26.24 ± 1.32[a]
Fx	23.84 ± 1.02	23.29 ± 1.13[bc]
Fx + HU	23.90 ± 0.84	22.74 ± 0.67[abc]
F value	0.222	24.53
p value	0.880	<0.001

Notes: Data are presented as mean ± standard deviation. a, vs. Baseline Weight (paired t-test); b vs. Sham; c, vs.HU, $p < 0.001$ (one-way ANOVA followed by Tukey's post hoc test) (n = 10 per group). Sham, sham control; Fx, fracture; HU, tail-suspension hindlimb unloading group; Fx + HU, fracture combined with tail-suspension hindlimb unloading group; ANOVA, one-way analysis of variance.

Expression and Correlation Analysis of Key Metabolites

Identification of key metabolites was performed by intersecting the results from differential metabolite screening with monotonic trend clusters identified via Mfuzz analysis. To evaluate expression levels and intergroup differences of key metabolites, hive plots were generated using the pcutils R package (v0.2.8). In addition, correlations among key metabolites were assessed by calculating correlation matrices, which were visualized using the corrplot R package (v0.95), a widely used method for metabolite correlation analysis.

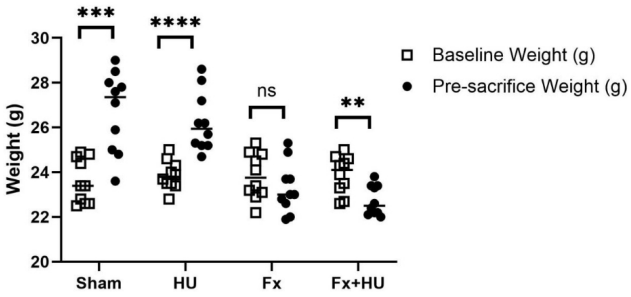

Fig. 3. Body weight changes in mice across different experimental groups. **$p < 0.01$, ***$p < 0.001$, ****$p < 0.0001$, ns: not significant.

Statistical Analysis

All statistical analyses were performed using SPSS software (version 26.0, IBM Corp., Armonk, NY, USA) and GraphPad Prism (version 9.0, GraphPad Software, San Diego, CA, USA). Quantitative data are presented as mean ± standard deviation (SD) for variables that met the as-

Table 2. Micro-CT quantitative analysis of trabecular bone parameters in different experimental groups.

Group	BMD (g/cm^3)	BV/TV (%)	Tb.Th (mm)	Tb.N (1/mm)	Tb.Sp (mm)
Sham	0.173 ± 0.013	21.9 ± 1.5	0.059 ± 0.003	3.29 ± 0.24	0.237 ± 0.022
HU	0.163 ± 0.012	20.5 ± 2.0	0.059 ± 0.002	3.17 ± 0.11	0.260 ± 0.043
Fx	0.165 ± 0.020	18.8 ± 2.2^{a}	0.058 ± 0.003	3.06 ± 0.23	0.260 ± 0.039
Fx + HU	0.129 ± 0.013^{abc}	12.7 ± 1.4^{abc}	0.053 ± 0.003^{abc}	2.72 ± 0.16^{abc}	0.390 ± 0.018^{abc}
F value	17.78	51.5	9.07	15.69	45.79
p value	<0.001	<0.001	<0.001	<0.001	<0.001

Notes: Data are presented as mean ± SD. a, vs. Sham, $p < 0.001$; b, vs. HU, $p < 0.001$; c, vs. Fx, $p < 0.001$ (one-way ANOVA followed by Tukey's post hoc test) (n = 10 per group). Micro-CT, micro-computed tomography; BMD, bone mineral density; BV/TV, bone volume fraction; Tb.Th, trabecular thickness; Tb.N, trabecular number; Tb.Sp, trabecular separation.

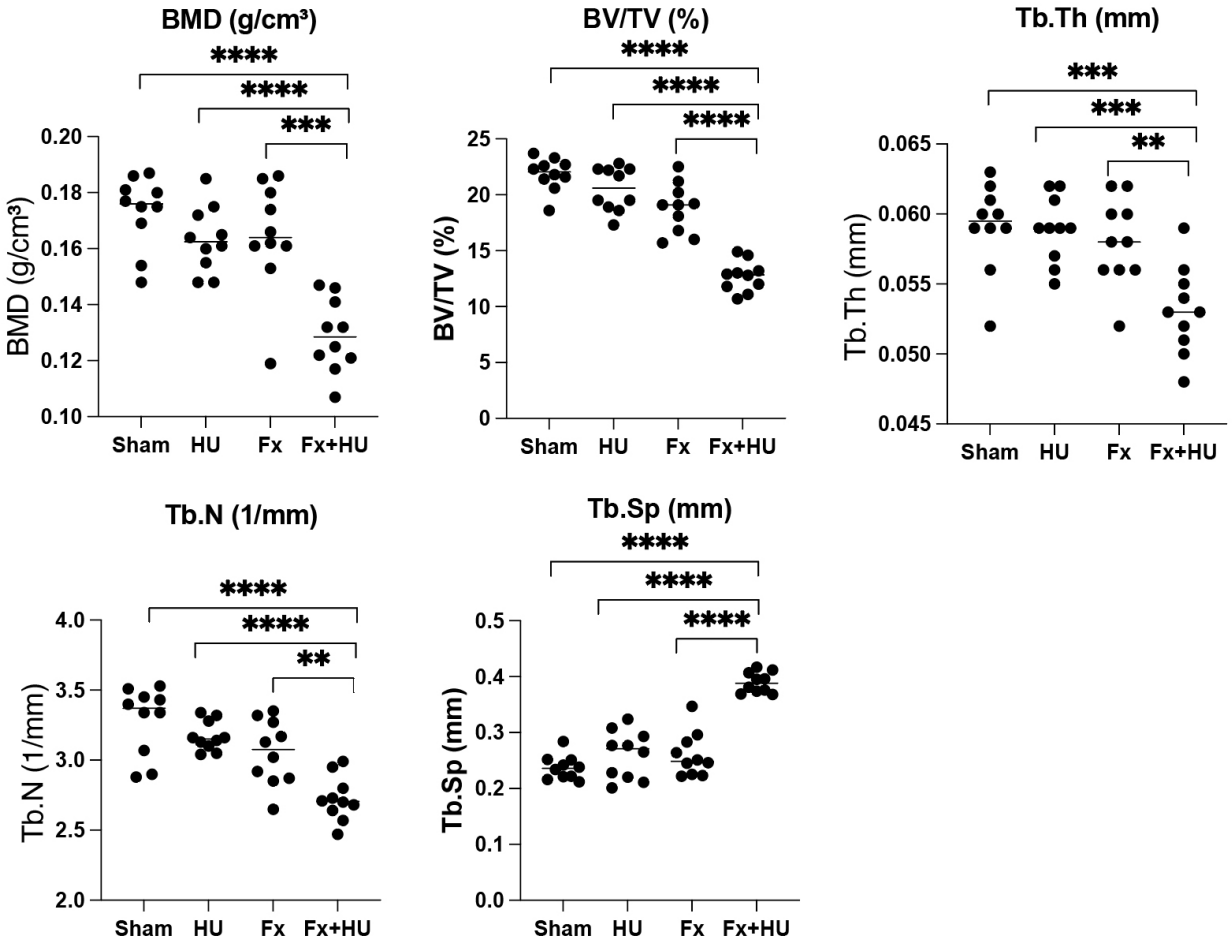

Fig. 4. Micro-CT quantitative analysis of trabecular bone parameters in different experimental groups. Micro-CT, micro-computed tomography. $^{**}p < 0.01$, $^{***}p < 0.001$, $^{****}p < 0.0001$.

sumptions of normality and homogeneity of variance. Normality was assessed using the Shapiro–Wilk test, and homogeneity of variance was assessed using Levene's test. For normally distributed data with equal variances, one-way analysis of variance (ANOVA) followed by Tukey's post hoc test was used for multiple group comparisons. Paired sample t test was used for comparison between the two groups. For data that did not meet these assumptions, non-parametric tests were applied using the Kruskal–Wallis test followed by Dunn's post hoc test. A two-sided p value < 0.05 was considered statistically significant.

Analyses were predefined with primary endpoints focused on micro-CT-derived trabecular bone parameters, including bone mineral density (BMD), bone volume fraction (BV/TV), trabecular thickness (Tb.Th), trabecular number (Tb.N), and trabecular separation (Tb.Sp). Metabolic pro-

filing analyses were considered exploratory endpoints, and multiple-testing procedures and variable importance measures were applied as appropriate in the multivariate analysis.

Results

Body Weight Changes Among Experimental Groups

After randomization, no statistically significant differences in body weight were observed among the groups before model establishment (one-way analysis of variance, $p > 0.05$), indicating good baseline comparability at the beginning of the experiment (Table 1 and Fig. 3).

Body weight was measured again prior to tissue harvesting. One-way ANOVA revealed significant differences in body weight among the experimental groups ($p < 0.001$). Further comparison of body weight distributions showed that the control group (Sham group) had a markedly higher overall body weight than the Fx, the HU, and the Fx + HU groups (Table 1 and Fig. 3). In contrast, body weight in all experimental groups was reduced to varying degrees compared with the control group (Table 1 and Fig. 3).

Fracture and Hindlimb Unloading Aggravated Trabecular Bone Loss and Microarchitectural Deterioration

Micro-CT quantitative analysis revealed significant alterations in trabecular bone mass and microarchitecture among the experimental groups (Table 2 and Fig. 4). One-way ANOVA demonstrated significant overall differences in BMD, BV/TV, Tb.Th, Tb.N, and Tb.Sp among the four groups (all $p < 0.001$, n = 10 per group).

Post hoc pairwise comparisons showed that, compared with the Sham group, both the Fx and HU groups exhibited impaired trabecular bone parameters, including reduced BMD, BV/TV, Tb.Th, and Tb.N, together with increased Tb.Sp (all $p < 0.05$ compared to Sham), for most parameters.

Notably, the Fx + HU group displayed the most severe deterioration in trabecular microarchitecture, characterized by the lowest BMD and BV/TV, further reductions in Tb.Th and Tb.N, and a pronounced increase in Tb.Sp. Consistent with the pairwise comparison results, the Fx + HU group differed significantly from both the Fx and HU groups across all trabecular parameters (Table 2; all $p < 0.05$ for Fx + HU vs. Fx, and Fx + HU vs. HU). These findings indicate that fracture and mechanical unloading exert additive adverse effects on trabecular bone microarchitecture.

Distinct Global Metabolic Profiles Were Observed Among the Four Experimental Groups

As shown in Fig. 5, principal component analysis (PCA) in the positive ion mode revealed minimal overlap among the sham, Fx, HU, and Fx + HU groups, indicating clear metabolic differences between groups subjected to different treatments. This distinct separation suggests good analytical stability and reproducibility of the metabolomic platform, and supports the reliability of the acquired data for subsequent analyses.

Furthermore, the fracture combined with Fx + HU was clearly separated from both the Fx and HU in the three-dimensional PCA score plots, indicating that the combined intervention induced pronounced alterations in the metabolic profiles compared with either intervention alone.

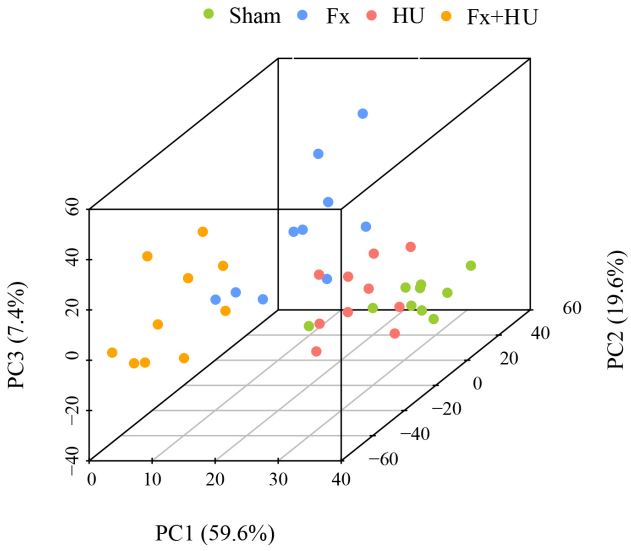

Fig. 5. PCA score plot in positive ion mode. Three-dimensional PCA score plots illustrate the distribution of metabolomic features among samples from the sham, Fx, HU, and Fx + HU groups. Different colors represent different experimental groups. The X-axis represents the metabolic feature index, while the Y- and Z-axes represent relative metabolite abundance. The X-axis represents PC1 (59.6%), while the Y- and Z-axes represent PC2 (19.6%) and PC3 (7.4%), respectively.

As shown in Fig. 6, orthogonal partial least squares discriminant analysis (OPLS-DA) performed in the positive ion mode revealed clear metabolic differences among the four experimental groups, indicating good overall data quality. The OPLS-DA model exhibited satisfactory predictive performance ($Q^2 > 0.5$), suggesting that the model was reliable.

Notably, in the three-dimensional OPLS-DA score plots, samples from the Fx + HU group were clearly separated from those of the HU group, indicating that mechanical unloading–associated metabolic profiles were significantly altered, and that the presence of fracture further modified the metabolic response under unloading conditions.

As shown in Fig. 7, principal component analysis (PCA) performed in the negative ion mode demonstrated minimal overlap among the sham, Fx, HU, and Fx + HU groups, indicating clear metabolic differences under the

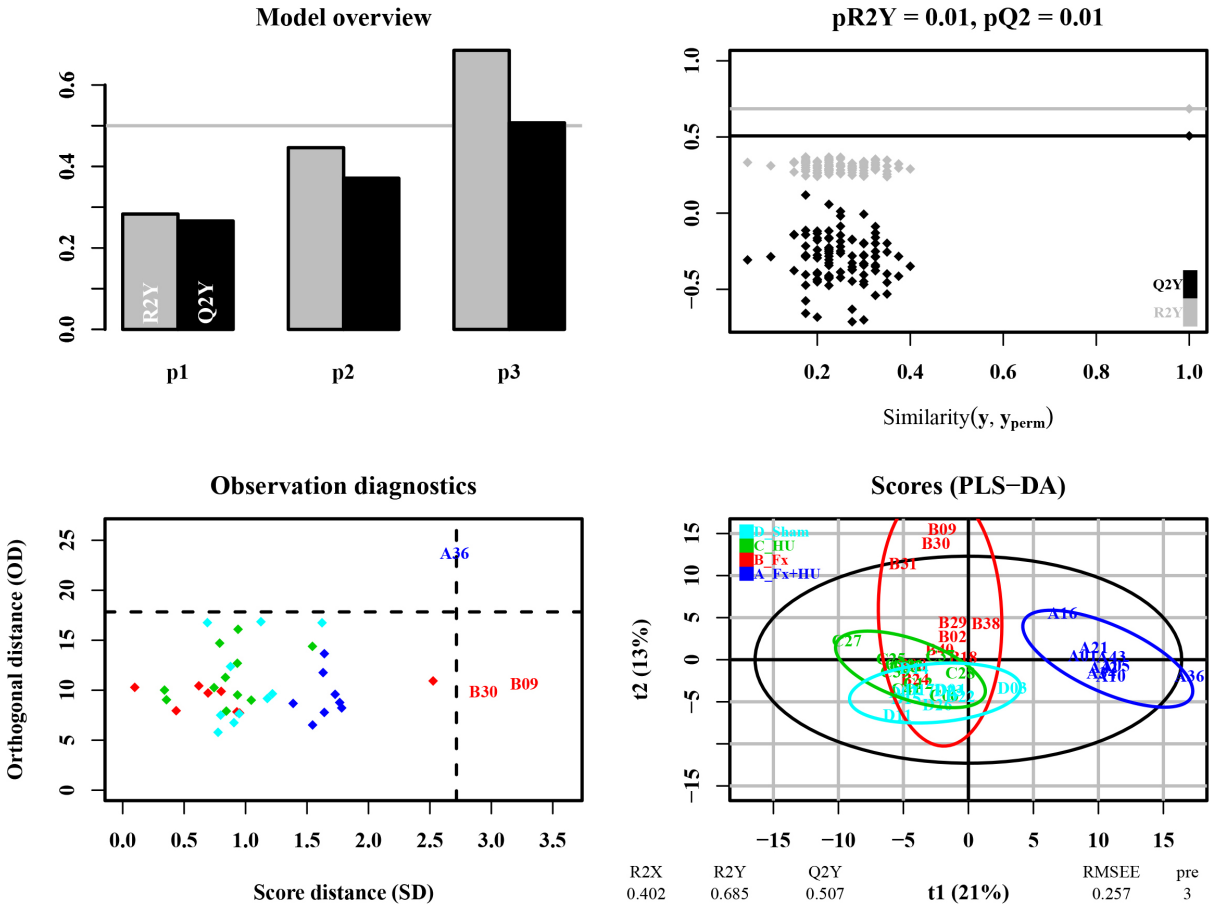

Fig. 6. OPLS-DA score plot in positive ion mode. The upper-left panel shows the scores of predictive components across dimensions, where p1 represents the predictive component; the cumulative explained variance is used to evaluate whether the orthogonal components are sufficient. The upper-right panel displays permutation test results of R2Y and Q2Y values for the actual and permuted models. When the permuted R2Y and Q2Y values (scatter points) exceed the corresponding values of the original model (horizontal lines), model overfitting is indicated. The horizontal axis represents the correlation coefficient between the original and permuted datasets, while the vertical axis represents R2Y and Q2 values. Black dots indicate Q2 values and gray dots indicate R2Y values; black and gray lines represent the regression lines of Q2 and R2Y, respectively. The lower-left panel shows the distribution of orthogonal distances, and the lower-right panel displays the coordinates of individual samples along the PLS-DA axes. Values of R2X, R2Y, and related parameters are shown below the plots to assess overall model fitness.

different experimental conditions. This separation suggests good analytical stability and reproducibility of the metabolomic platform, and supports the reliability of the acquired data for further analysis.

Moreover, samples from the Fx were clearly separated from those of the HU in the three-dimensional PCA score plots, indicating that fracture intervention significantly altered the metabolic profiles under negative ion detection conditions.

As shown in Fig. 8, orthogonal partial least squares discriminant analysis (OPLS-DA) in the negative ion mode revealed clear metabolic differences among the four experimental groups, indicating good overall data quality. The OPLS-DA model showed satisfactory predictive performance (Q^2 >0.5), suggesting robust model reliability.

In the three-dimensional score plots, samples from the Fx and Fx + HU groups were clearly separated from those of the HU group, indicating that both fracture and mechanical unloading significantly altered the metabolic profiles.

Differential Metabolite Identification

As shown in Fig. 9, in the positive ion mode, differential metabolite analysis revealed distinct changes among the experimental groups. Compared with the Fx group, the Fx + HU group exhibited 22 upregulated and 51 downregulated differentially expressed metabolites (DEMs). Compared with the HU group, the Fx + HU group showed 35 upregulated and 50 downregulated DEMs.

In addition, comparison between the Fx group and the Sham group identified 29 upregulated and 11 downregulated DEMs, while comparison between the HU group and

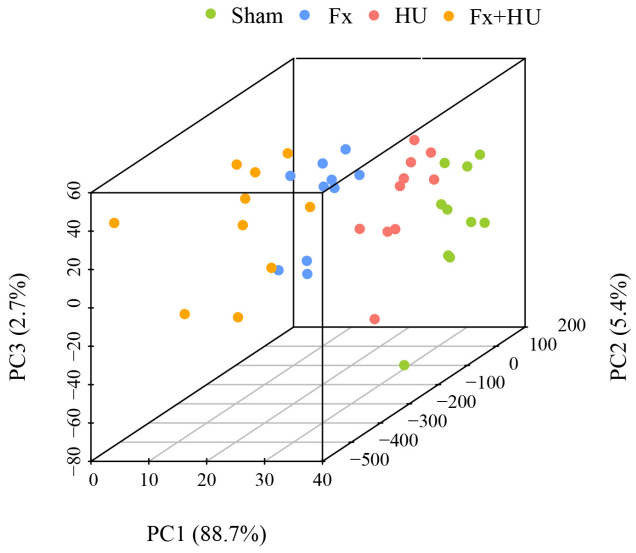

Fig. 7. PCA score plot in negative ion mode. Three-dimensional PCA score plots illustrate the distribution of metabolomic features among samples from the sham, Fx, HU, and Fx + HU groups, with different colors representing different experimental groups. The X-axis represents the metabolic feature index (Index), while the Y- and Z-axes represent relative metabolite abundance. The X-axis represents PC1 (88.7%), while the Y- and Z-axes represent PC2 (5.4%) and PC3 (2.7%), respectively.

the Sham group revealed 19 upregulated and 13 downregulated DEMs. These results are summarized in the corresponding figure.

As shown in Fig. 10, in the negative ion mode, differential metabolite analysis revealed marked differences among the experimental groups. Compared with the Fx group, the Fx + HU group exhibited 59 upregulated and 8 downregulated differentially expressed metabolites (DEMs). Compared with the HU group, the Fx + HU group showed 75 upregulated and 9 downregulated DEMs.

In addition, comparison between the Fx group and the Sham group identified 28 upregulated and 15 downregulated DEMs, while comparison between the HU group and the Sham group revealed 17 upregulated and 13 downregulated DEMs. These results are summarized in the corresponding figure.

KEGG Pathway Enrichment Analysis

As shown in Fig. 11, in the positive ion mode, KEGG pathway enrichment analysis was performed based on differentially expressed metabolites identified from multiple group comparisons. A total of 76 metabolites were identified in the Fx + HU vs Fx comparison, 87 metabolites in the Fx + HU vs HU comparison, 43 metabolites in the Fx vs Sham comparison, and 38 metabolites in the HU vs Sham comparison. Overall, these metabolites were enriched in 154 KEGG pathways, among which 43 pathways were significantly enriched ($p < 0.05$).

Specifically, 6 significantly enriched pathways were identified in the Fx + HU vs Fx comparison, 14 pathways in the Fx + HU vs HU comparison, 5 pathways in the Fx vs Sham comparison, and 18 pathways in the HU vs Sham comparison. Representative significantly enriched pathways included ATP-binding cassette (ABC) transporters, protein digestion and absorption, central carbon metabolism in cancer, and the mechanistic target of rapamycin kinase (mTOR) signaling pathway.

As shown in Fig. 12, in the negative ion mode, KEGG pathway enrichment analysis was conducted based on the identified differentially expressed metabolites. A total of 69 metabolites were identified in the Fx + HU vs Fx comparison, 85 metabolites in the Fx + HU vs HU comparison, 53 metabolites in the Fx vs Sham comparison, and 40 metabolites in the HU vs Sham comparison. Collectively, these metabolites were enriched in 275 KEGG pathways, among which 77 pathways were significantly enriched ($p < 0.05$).

Specifically, 13 significantly enriched pathways were identified in the Fx + HU vs Fx comparison, 22 pathways in the Fx + HU vs HU comparison, 21 pathways in the Fx vs Sham comparison, and 21 pathways in the HU vs Sham comparison. Representative enriched pathways included serotonergic synapse, biosynthesis of unsaturated fatty acids, and arachidonic acid metabolism (Mus musculus).

Metabolite Clustering Analysis

As shown in Fig. 13, in the positive ion mode, trend-based clustering analysis revealed distinct metabolite expression patterns among the experimental groups. In the comparison among the Fx + HU, Fx, and Sham groups, metabolites in cluster c2 exhibited a gradually increasing expression trend. In addition, in the comparison among the Fx + HU, HU, and Sham groups, metabolites in cluster c2 also showed a progressively increasing pattern.

As shown in Fig. 14, in the negative ion mode, within the comparison among the Fx + HU, Fx, and Sham groups, metabolites in cluster c3 displayed a gradually increasing expression trend, whereas metabolites in cluster c2 exhibited a gradually decreasing trend. Similarly, in the comparison among the Fx + HU, HU, and Sham groups, metabolites in cluster c1 showed a progressively increasing expression pattern, while metabolites in cluster c2 demonstrated a gradually decreasing trend.

Intersection and Key Metabolites

The analysis results are shown in the following figures. Figs. 15,16 show the overlapping metabolites identified across different group comparisons. Fig. 17 presents the metabolites shared by the comparisons among Fx + HU, Fx, and Sham groups, as well as those among Fx + HU, HU, and Sham groups, under both positive and negative ion modes.

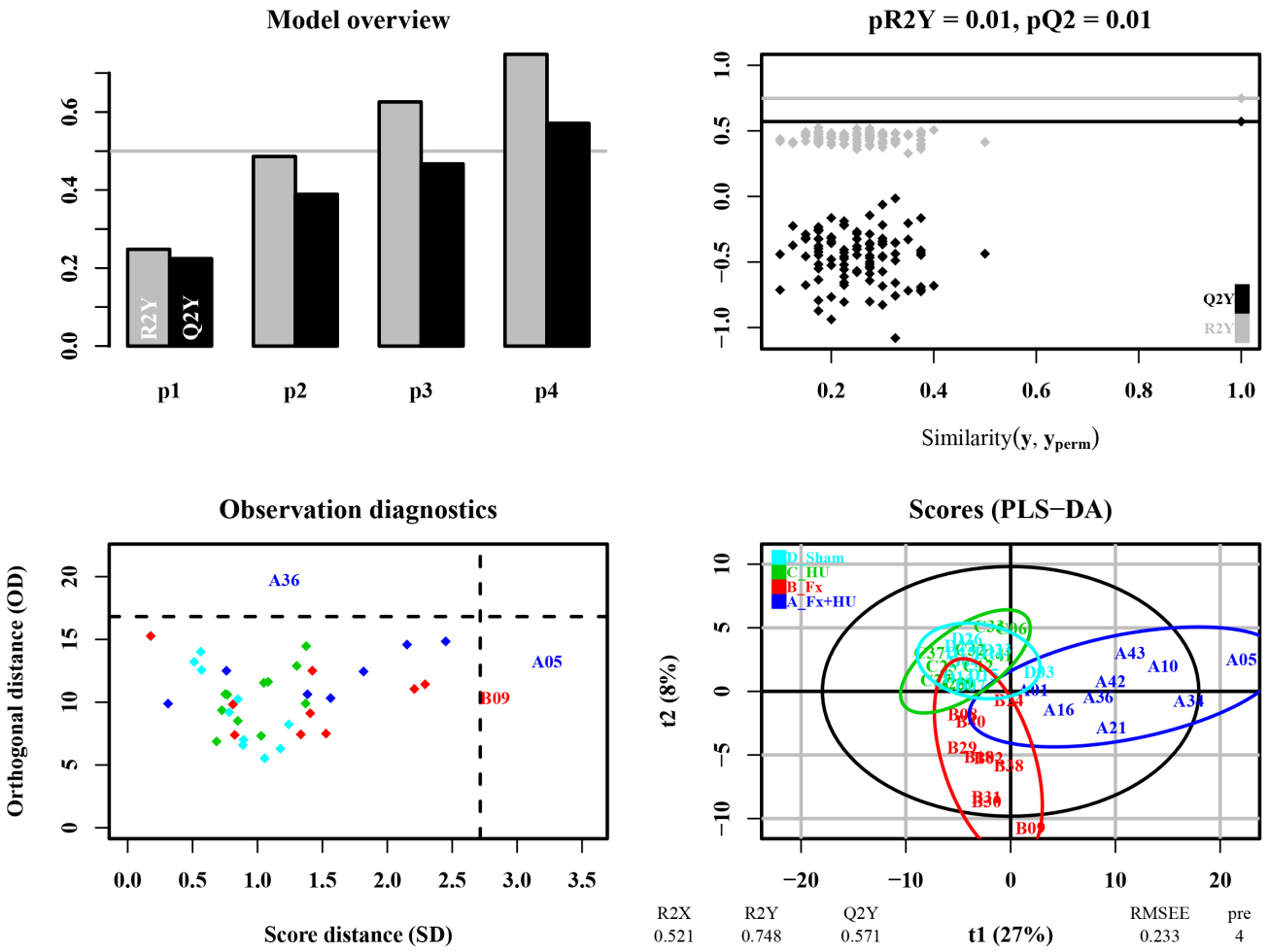

Fig. 8. OPLS-DA score plot in negative ion mode. The upper-left panel shows the scores of the predictive components across dimensions, where p1 represents the predictive component. The cumulative explained variance is used to evaluate whether the orthogonal components are sufficient.

In the negative ion mode, Allantoin was identified as a metabolite shared between these comparisons. Given that Allantoin is an ingredient with anti-inflammatory and healing-promoting properties, it likely primarily plays a role in promoting callus formation and accelerating endochondral ossification in this context. In addition, a comprehensive list of all key metabolites and their corresponding group classifications is provided in Table 3.

As shown in Fig. 18, in the positive ion mode, the levels of Tris(2,4-di-tert-butylphenyl) phosphate, PC(18:0/18:1(9Z)), and PC(P-18:0/18:1(9Z)) were consistently decreased in the Fx + HU, Fx, and HU groups. In contrast, in the negative ion mode, Hexanoylglycine, cis-11,14-eicosadienoic acid, Allantoin, Ribose, and Xylose were consistently increased in the Fx + HU, Fx, and HU groups.

As shown in Fig. 19, Tris(2,4-di-tert-butylphenyl) phosphate, PC(18:0/18:1(9Z)), and PC(P-18:0/18:1(9Z)) were negatively correlated with the other five metabolites. Among them, PC(18:0/18:1(9Z)) showed the strongest and most significant positive correlation with PC(P-18:0/18:1(9Z)) (cor = 0.97), whereas Tris(2,4-di-tert-butylphenyl) phosphate exhibited the strongest and most significant negative correlations with Allantoin, Ribose, and Xylose (cor = –0.66).

Table 3. Key metabolites identified in positive and negative ion modes.

		Comparison
1	Prostaglandin F2alpha	Sham-Fx-Fx+HU_NEG
2	cis-11.14-Eicosadienoic acid	Sham-Fx-Fx+HU_NEG
3	Hexanoylglycine	Sham-Fx-Fx+HU_NEG
4	Ribose	Sham-Fx-Fx+HU_NEG
5	Xylose	Sham-Fx-Fx+HU_NEG
6	PC(18:0/18:1(9Z))	Sham-Fx-Fx+HU_POS
7	PC(P-18:0/18:1(9Z))	Sham-Fx-Fx+HU_POS
8	Prostaglandin F2alpha	Sham-HU-Fx+HU_NEG
9	Tris(2,4-di-tert-butylphenyl)phosphate	Sham-HU-Fx+HU_POS

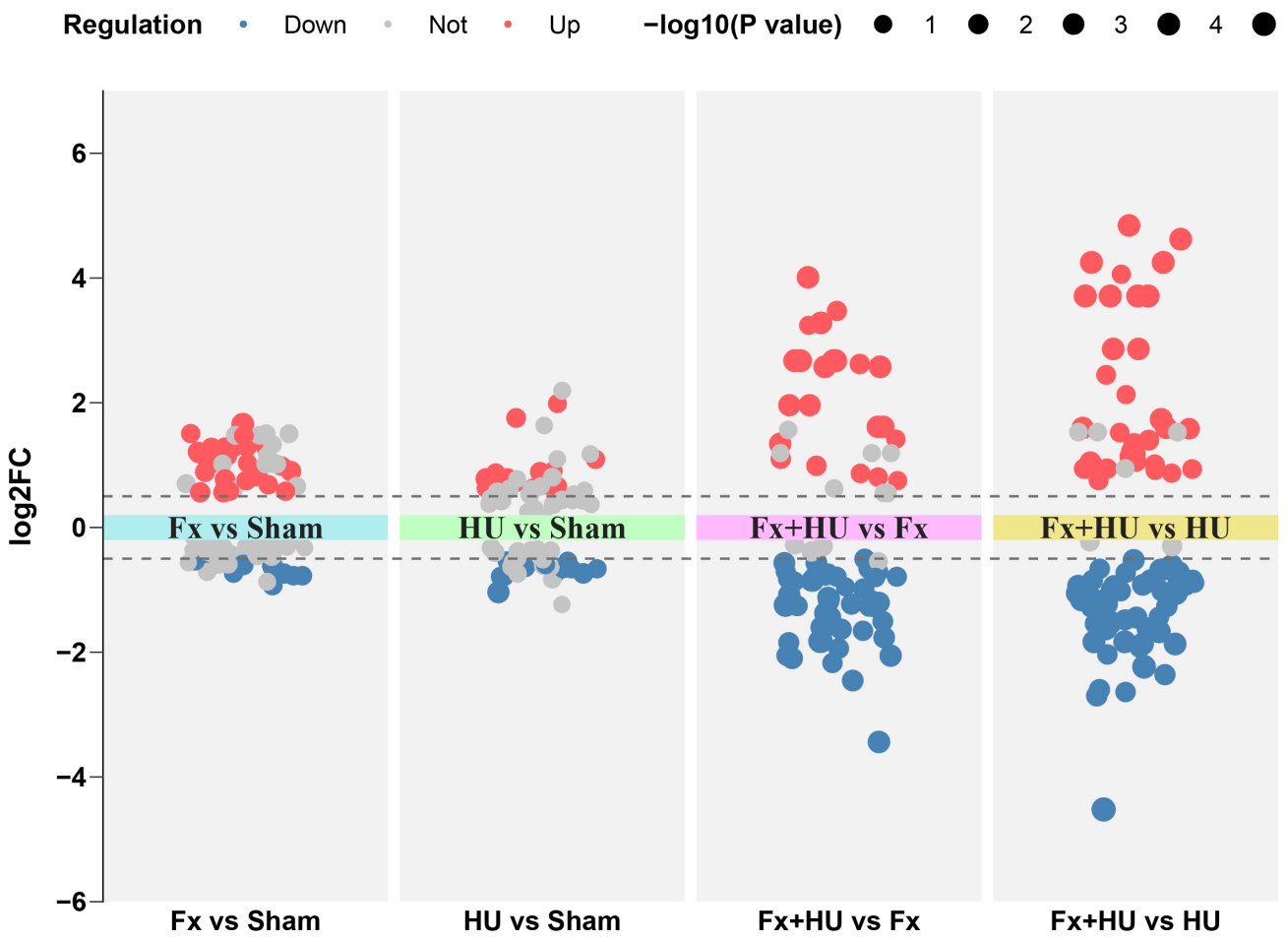

Fig. 9. Volcano plots of differential metabolite expression among different groups in positive ion mode. Notes: The y-axis (log_2 fold change, log_2FC) represents the logarithmic fold change of metabolite abundance between two groups, where positive values indicate significantly upregulated metabolites and negative values indicate significantly downregulated metabolites. The x-axis ($-log_{10}$ *p*-value) represents the negative logarithm of the statistical significance, with larger values indicating greater significance of differential expression. Red dots indicate significantly upregulated metabolites and blue dots indicate significantly downregulated metabolites, defined by the preset screening criteria (absolute log_2 fold change >1 and $p < 0.05$). Gray dots indicate metabolites that did not meet these criteria.

Discussion

The untargeted metabolomic analysis in this study systematically delineated the bone tissue metabolic profiles of mice under three distinct conditions: fracture (Fx), hindlimb unloading (HU), and their combination (Fx + HU). Our most critical finding is that the metabolic reprogramming induced by Fx+HU is not a simple summation of the individual effects of Fx or HU, but rather manifests as a unique metabolic fingerprint. Multivariate statistical analyses (PCA and PLS-DA) revealed clear separation among all four groups, confirming that each intervention elicited a distinct systemic metabolic response. Notably, the Fx+HU group was significantly distinguished from both the Fx and HU groups under both positive and negative ion modes, indicating the activation of a novel regulatory network specific to combined mechanical insult and disuse. Through stringent filtering criteria, we identified a panel of differentially abundant metabolites and enriched pathways, among which dysregulation in arachidonic acid metabolism, amino acid metabolism (particularly branched-chain amino acids), and phospholipid metabolism likely constitute the core metabolic mechanisms underlying the synergistic impairment of bone metabolism.

Prior to addressing the combined effects, it is essential to elucidate the mechanism of unloading alone. In our HU model, significant reductions in bone microstructural parameters—bone mineral density (BMD), bone volume/total volume (BV/TV), and trabecular thickness (Tb.Th)—were observed compared to sham controls, consistent with prior literature [30]. Recent advances highlight osteocytes, the primary mechanosensors in bone, as central players in metabolic reprogramming under mechanical unloading. Liu *et al.* [21] demonstrated that HU induces a shift in osteocyte energy metabolism via the hypoxia inducible factor 1 subunit alpha (HIF1A)/pyruvate

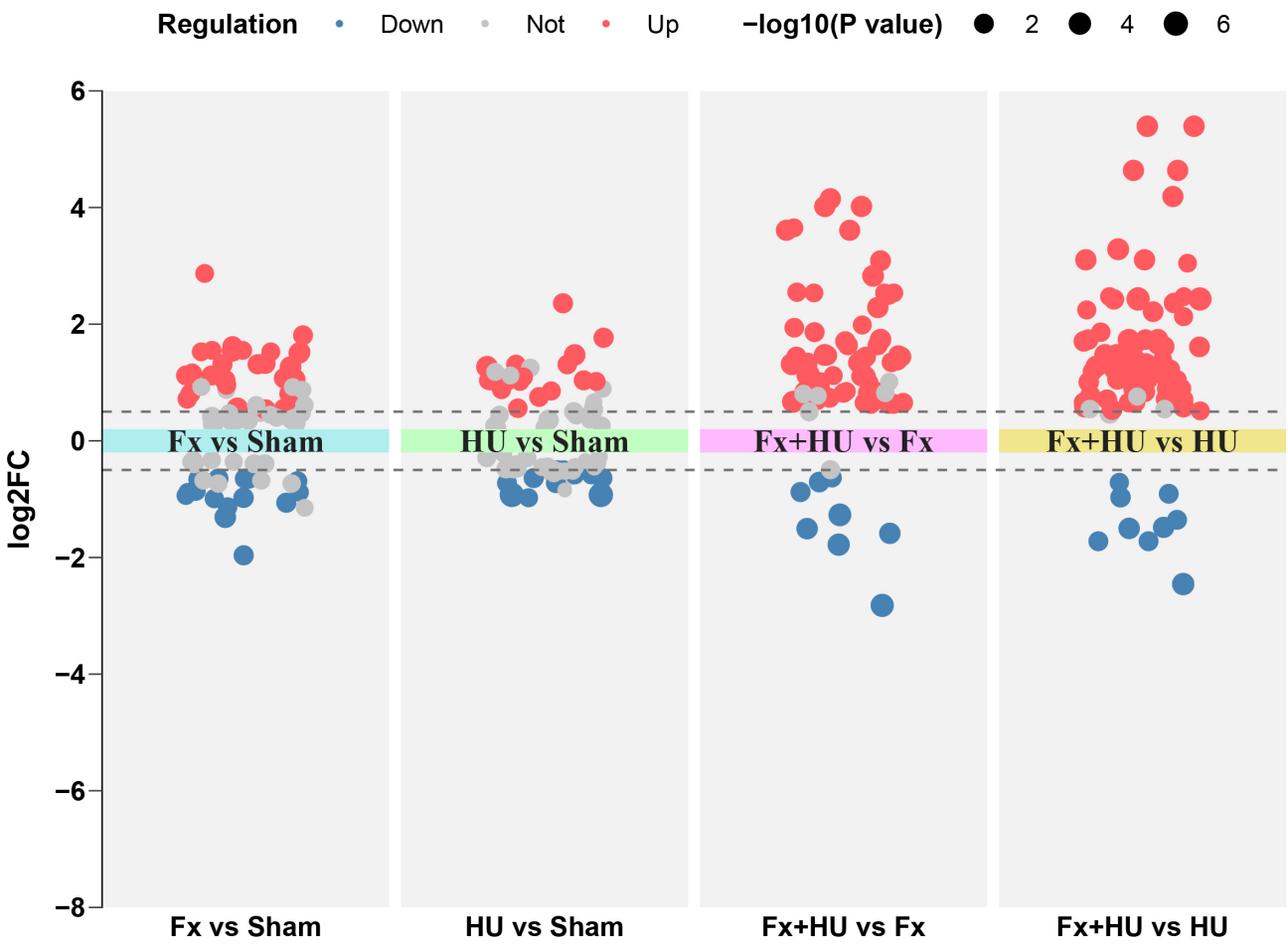

Fig. 10. Volcano plots of differential metabolite expression among different groups in negative ion mode. Notes: The y-axis (log_2 fold change, log_2FC) represents the logarithmic fold change of metabolite abundance between two groups, where positive values indicate significantly upregulated metabolites and negative values indicate significantly downregulated metabolites. The x-axis ($-log_{10}$ *p*-value) represents the negative logarithm of the statistical significance, with larger values indicating greater significance of differential expression. Red dots indicate significantly upregulated metabolites and blue dots indicate significantly downregulated metabolites, defined by the preset screening criteria (absolute log_2 fold change >1 and $p < 0.05$). Gray dots indicate metabolites that did not meet these criteria.

dehydrogenase kinase 1 (PDK1) axis, upregulating glycolysis and transcriptionally inducing glutaminase 2 (GLS2), thereby establishing a state of glutamine addiction. This metabolic dependency compromises ATP synthesis and disrupts calcium oscillation dynamics, ultimately impairing the osteocyte's ability to sense mechanical stimuli [21]. This paradigm shifts the understanding of disuse-induced bone loss from a passive "use-it-or-lose-it" phenomenon to an active reprogramming of cellular bioenergetics that fundamentally alters skeletal mechanosensitivity. The decline in bone mechanical properties observed in our HU group aligns precisely with this mechanistic framework.

In negative ion mode, the arachidonic acid (AA) metabolic pathway was significantly enriched in the Fx + HU group compared with all other groups. AA is a crucial component of cell membrane phospholipids, and it is metabolized via pathways involving cyclooxygenase (COX) and lipoxygenase (LOX) to generate a series of biologically active eicosanoids, such as prostaglandins and leukotrienes. These substances are key signaling molecules that regulate inflammation and bone metabolism. Studies have shown that the AA metabolic pathway plays an important role in the development and progression of osteoporosis. For example, aucubin improves glucocorticoid-induced osteoporosis in mice by regulating AA metabolism [31], suggesting that targeting AA metabolism may be an effective strategy for treating metabolic bone diseases.

Our data showed that, compared with the Sham group, the levels of various prostaglandins in the Fx and HU groups showed a downward trend. This may reflect a negative feedback regulation mechanism in the body after initial trauma or stress, aimed at controlling excessive inflammation. However, notably, in the Fx + HU group, the level of prostaglandin F2α (PGF2α) was significantly upregulated and identified as a key metabolite connecting the two change trends of Sham-Fx-Fx+HU and Sham-HU-Fx+HU.

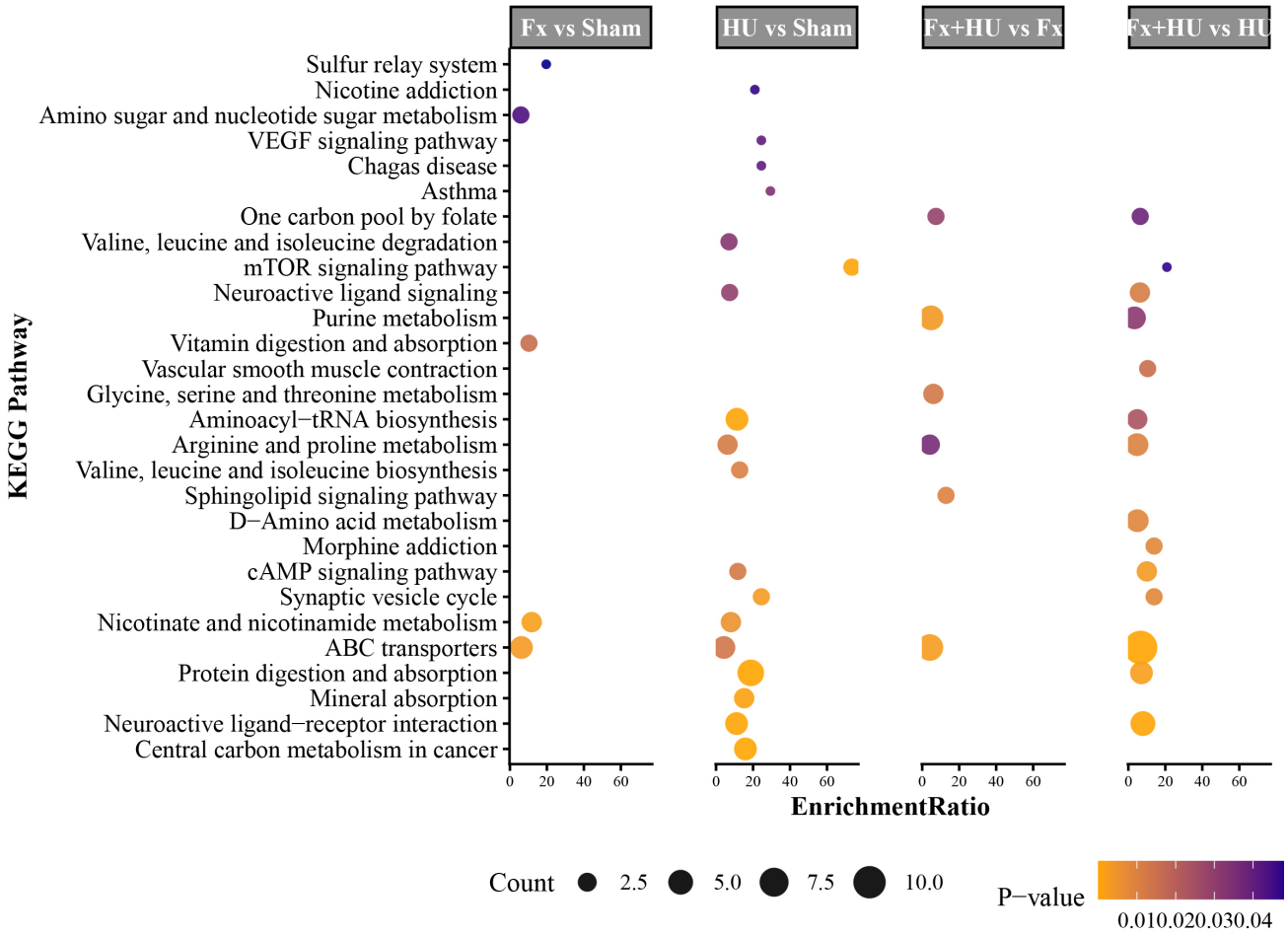

Fig. 11. KEGG pathway enrichment of differential metabolites in positive ion mode. The x-axis indicates the enrichment ratio, and the y-axis lists KEGG pathways. Dot size corresponds to the number of enriched metabolites, and color reflects the *p*-value, with warmer colors indicating higher significance. KEGG, Kyoto Encyclopedia of Genes and Genomes.

Kuroyanagi *et al.* [32] showed that in osteoblasts, PGF2α can induce the phosphorylation of mitogen-activated protein kinase (MAPK) and MAPK8, thereby regulating the secretion of IL-6. The specific increase in PGF2α in the Fx + HU group strongly suggests that combined intervention may redirect the inflammatory response towards a direction that promotes bone resorption by activating specific prostaglandin synthesis pathways, thereby exacerbating bone loss. This is highly consistent with the clinical observation that patients with fractures combined with immobilization experience rapid callus resorption and severe osteoporosis.

KEGG enrichment analysis in positive ion mode showed that ABC transporters, amino acid biosynthesis, and the mTOR signaling pathway were significantly enriched in the Fx + HU group compared with other groups. mTOR is a core kinase in cells that senses nutritional and energy status, regulates protein synthesis and cell growth, and is crucial for bone formation [33]. Branched-chain amino acids (BCAAs), especially leucine, are effective activators of mTOR. A review by Liang *et al.* [34] systematically summarized the role of BCAAs in bone metabolism, highlighting that BCAAs affect bone remodeling through multiple processes, including regulation of the activity of osteoblasts and osteoclasts, participation in energy sensing, oxidative stress, and immune regulation. Our results showed that in the comparison between the HU and Sham groups, the levels of leucine, isoleucine, and valine were significantly downregulated, while the mTOR signaling pathway was enriched. This suggests that unloading alone may inhibit mTOR activity by reducing amino acid supply, thereby leading to a decrease in bone formation. However, in the comparison between the Fx + HU and HU groups, we found that the level of valine was instead upregulated. This seemingly contradictory phenomenon precisely reveals the complexity of combined intervention. We speculate that this may be a compensatory response: fracture trauma itself requires substantial protein and energy for tissue repair, and the body may increase circulating amino acids (including valine) by mobilizing muscle protein breakdown to meet the anabolic demands of the liver and fracture site. However, this approach may lead to muscle atrophy and sys-

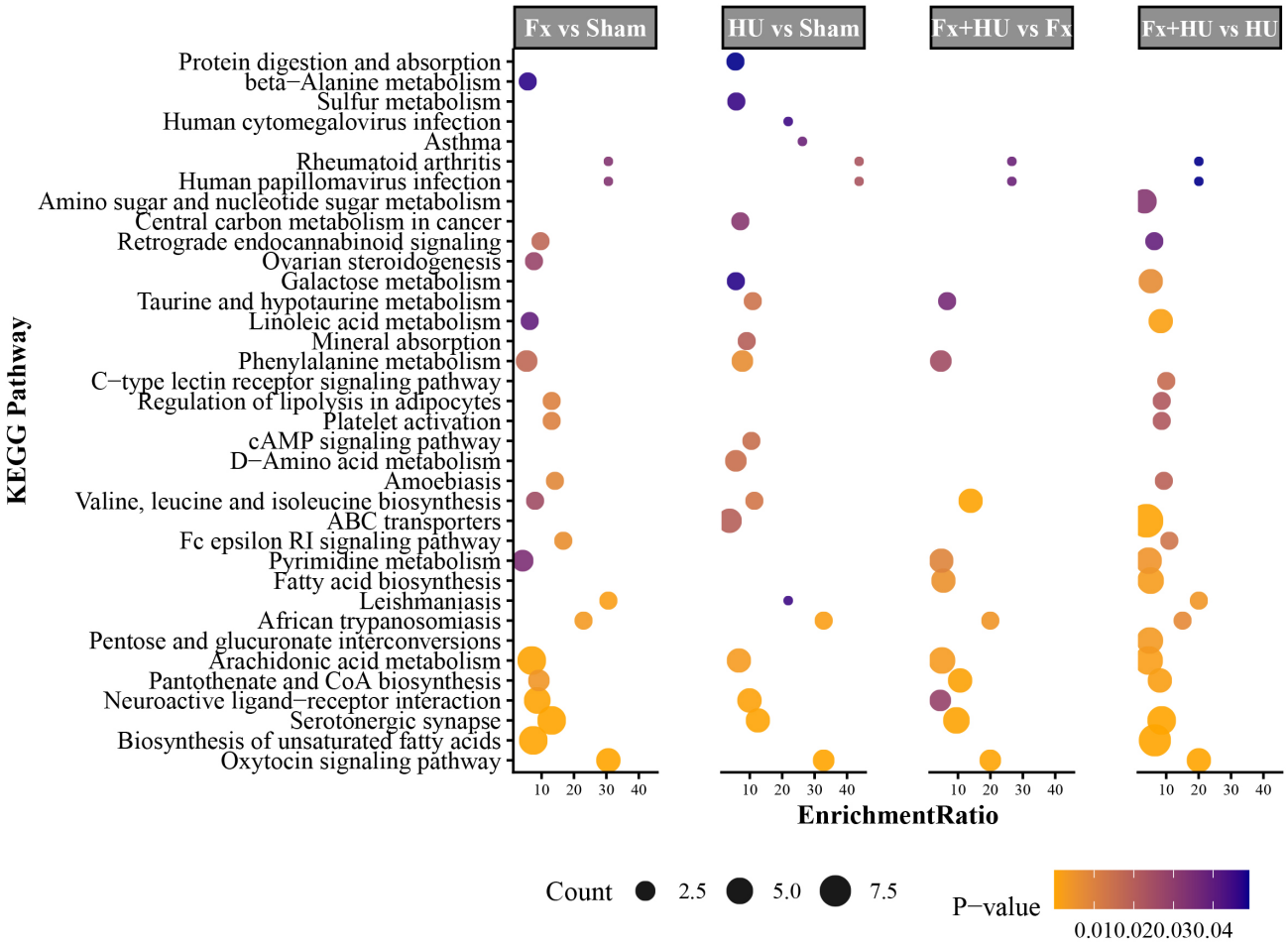

Fig. 12. KEGG pathway enrichment of differential metabolites in negative ion mode. The x-axis indicates the enrichment ratio, and the y-axis lists KEGG pathways. Dot size corresponds to the number of enriched metabolites, and color reflects the *p*-value, with warmer colors indicating higher significance.

temic metabolic disorders in the long run. In fact, the interaction between muscle and bone (muscle-bone crosstalk) has become a research hotspot in osteoporosis, and the regulation of bone metabolism by muscle-derived metabolites and cytokines deserves further in-depth exploration.

In positive ion mode, multiple phosphatidylcholines (PCs), such as PC(18:0/18:1(9Z)) and PC(P-18:0/18:1(9Z)), were significantly downregulated in the Fx + HU group and were identified as key metabolites. Phospholipids are the basic skeleton of cell membranes and also a reservoir of signaling molecules (such as AA). The downregulation of PCs may reflect enhanced dynamic remodeling or structural damage of cell membranes under the dual stress of fracture and unloading. Lipid metabolism plays an important role in age-related musculoskeletal diseases, and lipid metabolism disorders can exacerbate bone loss and muscle atrophy by affecting fatty acid uptake, lipid signal transduction, and lipotoxicity [35]. On the one hand, inflammatory responses and oxidative stress may promote peroxidation and degradation of membrane phospholipids; on the other hand, the body may mobilize phospholipids as an energy source or use their decomposition products (such as lysophospholipids) as signaling molecules to participate in the repair process. Research by Kang *et al.* [36] revealed the dual role of phosphatidylserine and its receptors in osteoclast formation, further confirming the close association between phospholipid metabolism and bone resorption. Correlation analysis showed that these downregulated PCs were significantly negatively correlated with upregulated metabolites such as PGF2α and ribose, suggesting that the decomposition of membrane phospholipids may be closely functionally coupled with the production of inflammatory signals (release of AA) and the activation of energy metabolism (ribose participates in the pentose phosphate pathway).

In recent years, the role of mitochondrial function in the regulation of bone metabolism has received increasing attention. Research showed that mitophagy-related proteins BCL2 interacting protein 3 (BNIP3) and BNIP3L play key roles in regulating energy metabolism and mitochondrial stress signal transduction in osteocytes, and their deletion can lead to decreased bone mineral density and impaired

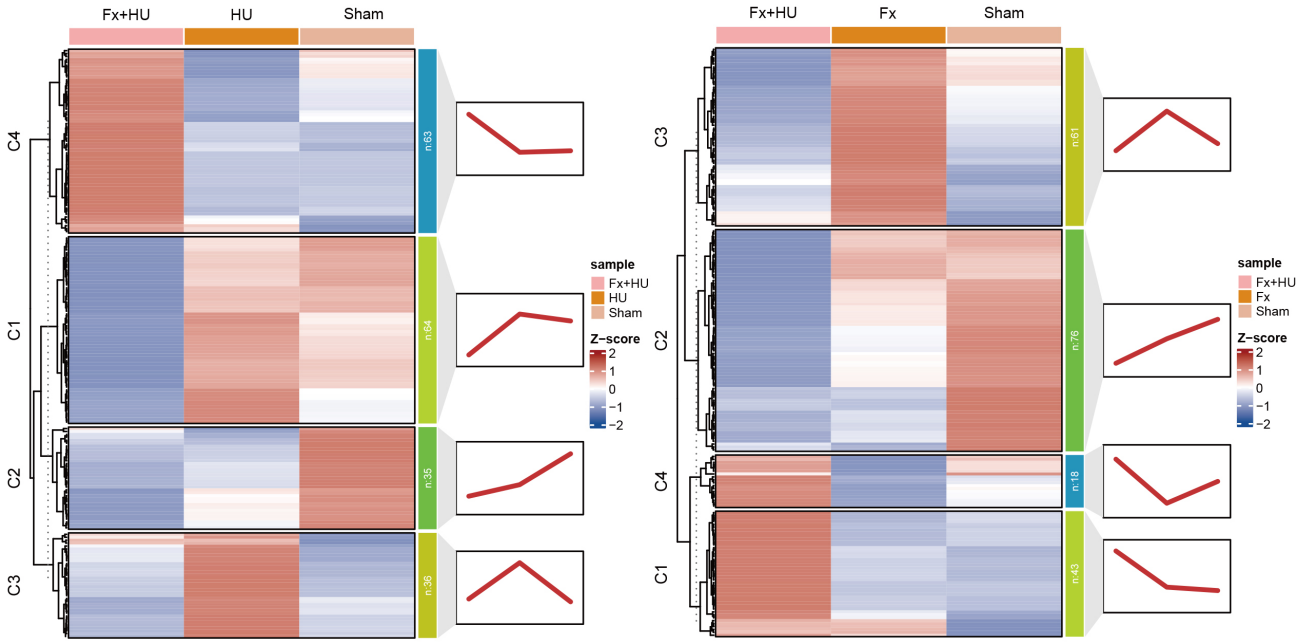

Fig. 13. Mfuzz clustering heatmap of metabolites among different groups in positive ion mode. Notes: The clusters are shown on the left, with each cluster representing a group of metabolites sharing similar expression patterns. In the central heatmap, colors from blue to white to red indicate increasing metabolite abundance. Each row represents a metabolite, and each column represents a sample, visually illustrating differences in metabolite expression across samples and the overall expression patterns after clustering. The line plots on the right correspond to the clusters on the left (C1–C4) and display the average expression trends of all metabolites within each cluster.

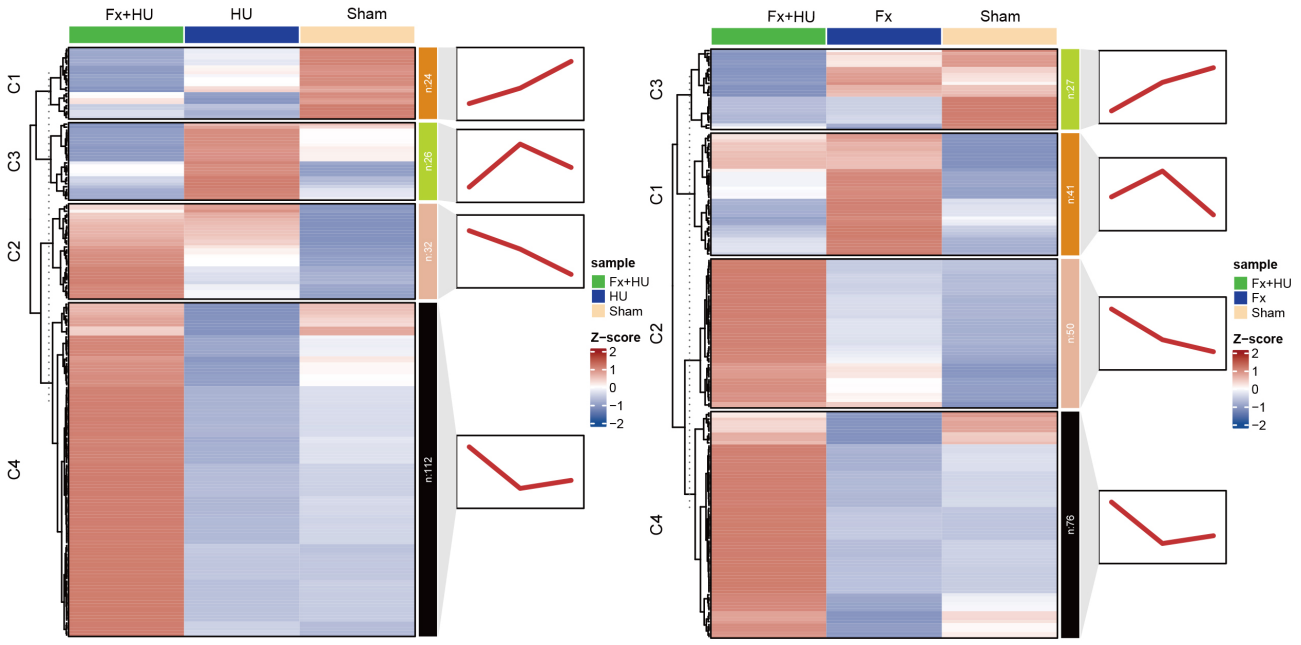

Fig. 14. Mfuzz clustering heatmap of metabolites among different groups in negative ion mode. Notes: The clusters are shown on the left, with each cluster representing a group of metabolites sharing similar expression patterns. In the central heatmap, colors ranging from blue to white to red indicate increasing metabolite abundance. Each row represents a metabolite, and each column represents a sample, visually illustrating differences in metabolite expression across samples and the overall expression patterns after clustering. The line plots on the right correspond to the clusters on the left (C1–C4) and display the average expression trends of all metabolites within each cluster.

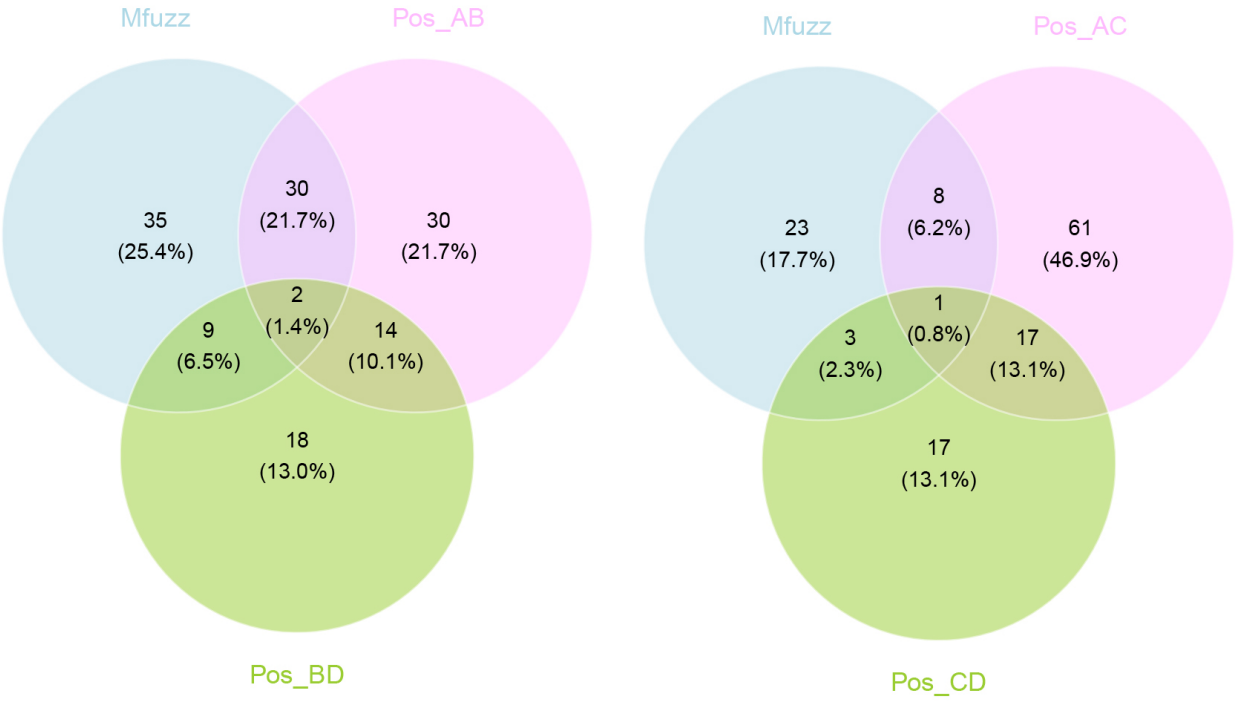

Fig. 15. Venn diagram of key metabolites in positive ion mode.

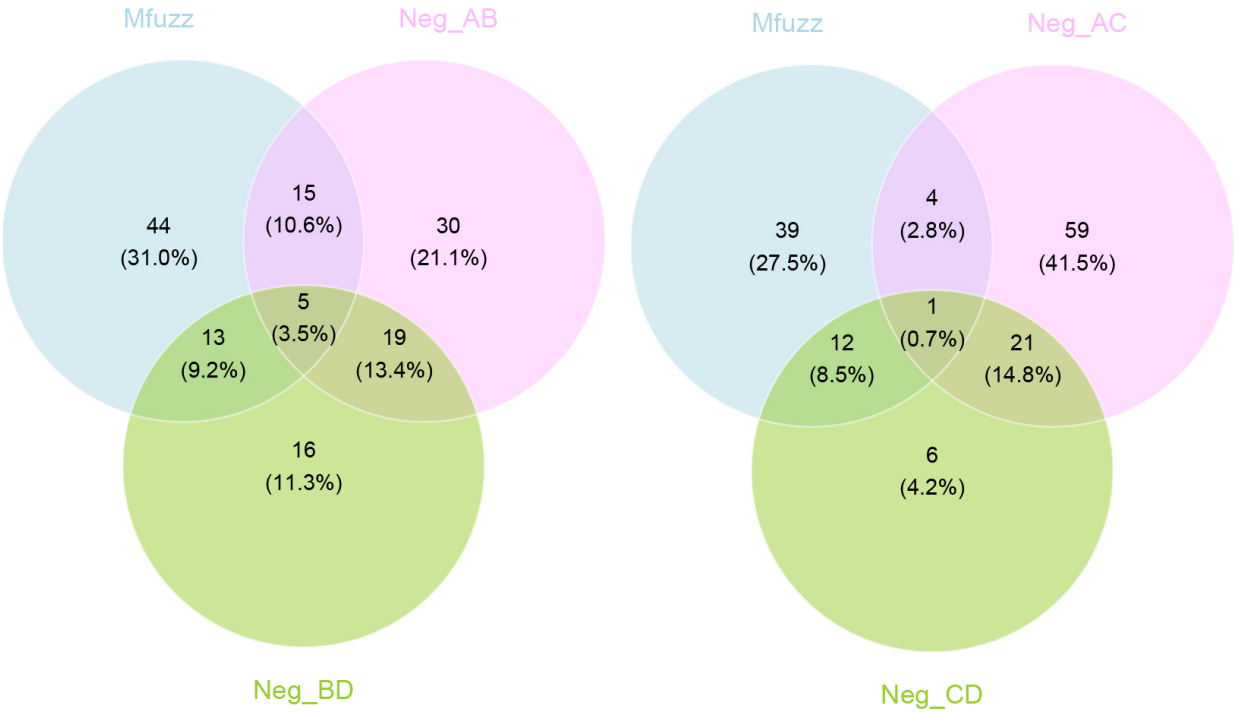

Fig. 16. Venn diagram of key metabolites in negative ion mode.

fracture healing [37]. In addition, parathyroid hormone (PTH) can affect glycolytic metabolism and the formation of mitochondria-derived vesicles in osteoblasts, suggesting a close connection between hormone regulation and energy metabolism [38]. In this study, the increased levels of ribose and xylose in the Fx + HU group may reflect the activation of the pentose phosphate pathway, which not only provides substrates for nucleotide synthesis but also produces NADPH for antioxidant defense. Under conditions of enhanced oxidative stress, the upregulation of the pentose phosphate pathway may be a protective adaptation of cells. The vicious cycle between mitochondrial dysfunction

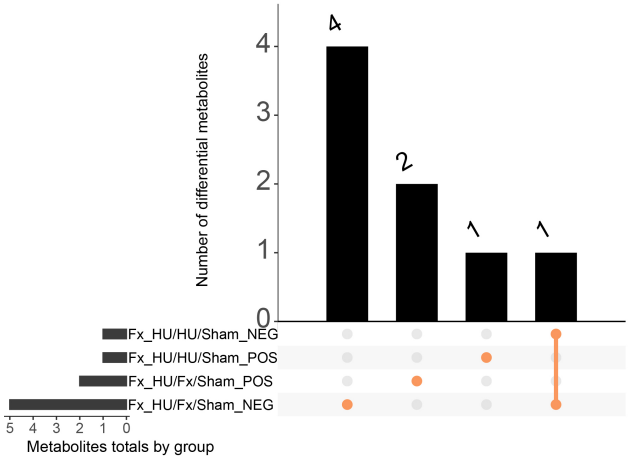

Fig. 17. UpSet plot of metabolites in positive and negative ion modes.

and oxidative stress has been proven to play an important role in the pathogenesis of osteoporosis.

This study adopted a strategy of non-targeted metabolomics combined with multivariate statistical analysis to systematically compare the differences in metabolic profiles among four groups of mice. PCA analysis in positive and negative ion modes showed that the four groups of samples were clearly clustered with low overlap, and the Fx + HU group was significantly separated from the Fx and HU groups. The Q^2 values of the PLS-DA and OPLS-DA models were both greater than 0.5 without overfitting, indicating that fracture and unloading alone or in combination can reshape the metabolic profile, and the combined intervention has a stronger disturbance and unique regulatory effect. Differential metabolites screened based on VIP >1, $|\log_2 FC| > 0.5$, and $p < 0.05$ were heterogeneously distributed in positive and negative ion modes. KEGG enrichment analysis showed that they were primarily involved in pathways such as substance transport, energy metabolism, and signal transduction. The advantage of this multi-omics integrated analysis strategy is that, on the one hand, differential metabolites discovered through metabolomics can serve as "anchors" to guide subsequent molecular mechanism research; on the other hand, changes in metabolic pathways can reflect the body's overall response to intervention, providing a system-level perspective for understanding complex pathological processes.

In addition, this study has certain limitations. First, the results of untargeted metabolomics mainly reflect correlations among metabolites and cannot directly establish causal relationships. Subsequent studies need to verify our proposed mechanism hypotheses through targeted metabolomics, *in vitro* cell experiments, or *in vivo* intervention experiments (such as using inhibitors of specific pathways). Second, this study analyzed metabolites in proximal tibial bone tissue rather than serum. Although this tissue-based approach better reflects the local skeletal microenvironment, it does not fully capture metabolic changes in other tissues or in the circulation. Future studies integrating bone tissue metabolomics, serum metabolomics, and transcriptomics may provide a more comprehensive understanding of the regulatory network underlying bone loss after fracture and unloading. Third, the sample size was relatively limited, and some results need to be verified in a larger sample size. Fourth, this study primarily focused on metabolite alterations, and subsequent research should integrate proteomic and transcriptomic data to construct a more comprehensive regulatory network. Fifth, the animal model used in this study involved young adult mice, while clinically, acute bone loss after fractures is more common in the elderly population in clinical settings. Future studies should therefore validate the findings of this study in aged animal models. Sixth, another limitation of the present study is the lack of secondary molecular validation for the key metabolites and pathways identified by untargeted metabolomics. Therefore, the current findings should be interpreted as hypothesis-generating rather than definitive mechanistic evidence. Future research should verify representative pathways at the molecular, cellular and *in vivo* levels, such as lipid metabolism and amino acid metabolism-related signals. In addition, it is noteworthy that the reduced pre-sacrifice body weight observed in some groups, particularly in the Fx + HU group, may have contributed to the observed metabolic alterations. Therefore, a contribution of overall physiological stress and weight loss to the metabolic phenotype cannot be excluded. Nevertheless, the concurrent micro-CT evidence of marked trabecular deterioration supports a substantial skeletal effect of fracture and unloading. This potential confounding factor should be considered when interpreting the metabolomic findings.

In summary, this study is the first to systematically characterize the bone tissue metabolic profile of mice under conditions of fracture combined with unloading, revealing a unique pattern of metabolic remodeling. Our results indicate that combined intervention is not a linear superposition of the effects of single interventions, but rather couples inflammatory responses, energy metabolism, and cell homeostasis regulation through the interaction of three core networks: arachidonic acid metabolism, amino acid/mTOR signaling, and phospholipid metabolism, ultimately exacerbating the imbalance between bone formation and bone resorption. The key metabolites identified in this study, especially PGF2α and phospholipid molecules, may serve as potential biomarkers for predicting the risk of bone loss in patients with fractures combined with immobilization and provide a new theoretical basis for the development of therapeutic strategies targeting specific metabolic pathways. The disturbance of the metabolic network in mice by combined intervention of fracture and unloading is more significant than that of single intervention, and the regulatory effect has ion specificity and pathway selectivity.

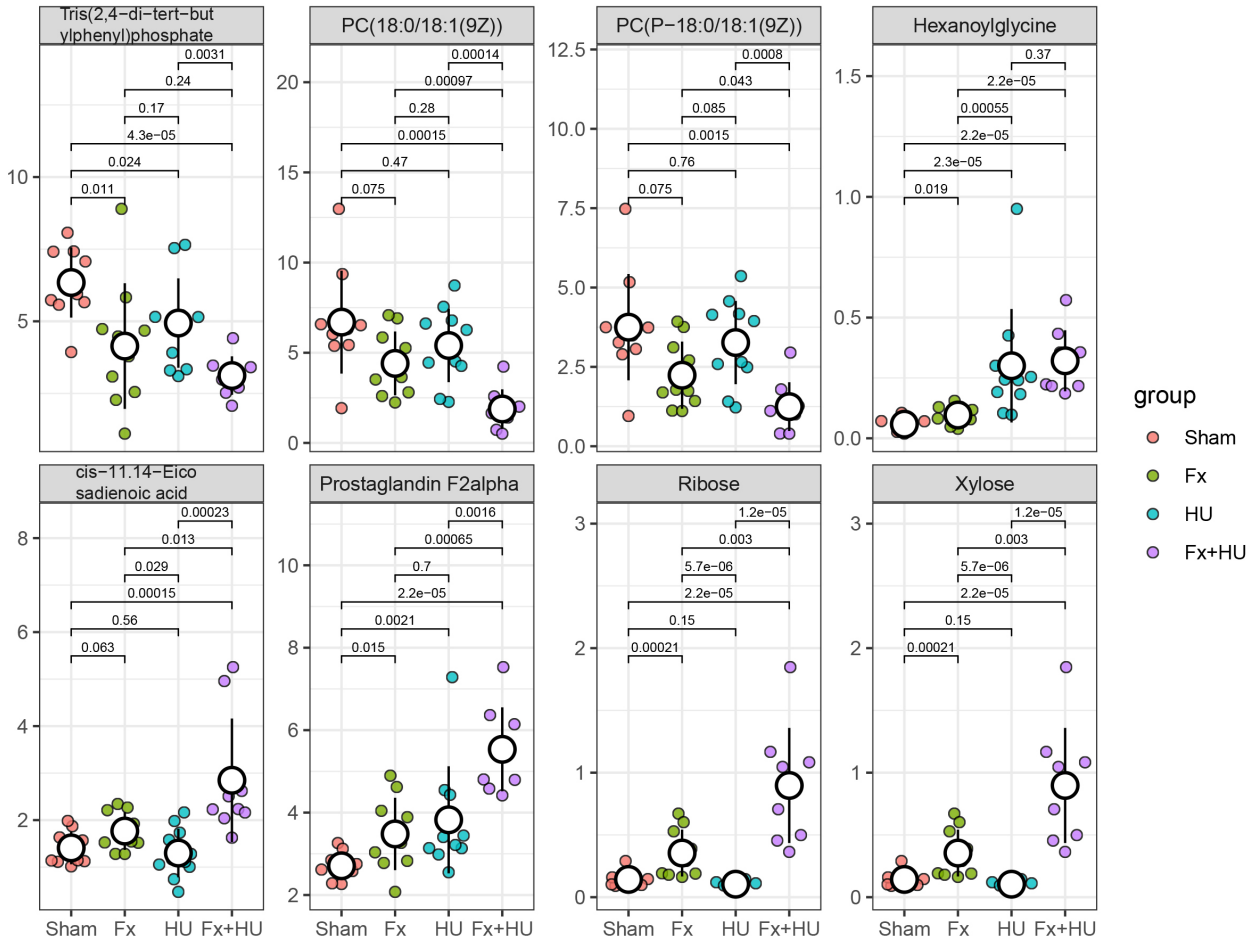

Fig. 18. Beehive plots of key metabolite expression levels in positive and negative ion modes.

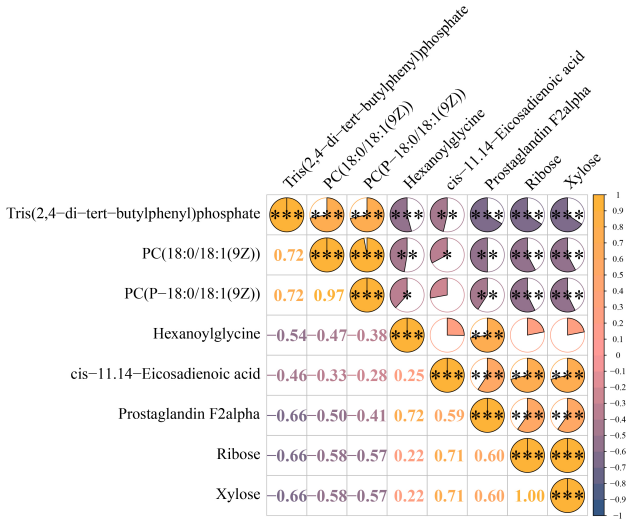

Fig. 19. Correlation analysis of key metabolite expression levels in positive and negative ion modes. $*p < 0.05$, $**p < 0.01$, $***p < 0.001$.

By targeting key pathways and metabolites, it synergistically affects processes such as substance transport, inflammatory response, and tissue repair, providing experimental support for the screening of bone repair-related biomarkers and the development of therapeutic strategies. This study provides experimental evidence for understanding the metabolic mechanism underlying the combined effect of fracture and mechanical stress, and also provides new insights for the identification of bone repair-related biomarkers and the development of therapeutic strategies.

Conclusions

Fracture and hindlimb unloading each induced substantial alterations in trabecular bone microarchitecture and bone tissue metabolic profiles, whereas their combination produced the most severe structural deterioration and the greatest metabolic divergence. The altered metabolites and enriched pathways were primarily associated with amino acid metabolism, lipid metabolism, energy metabolism, and oxidative stress-related processes. These findings suggest that fracture combined with mechanical unloading induces a distinct pattern of metabolic remodeling rather than a simple additive effect of either condition alone, and may provide candidate metabolic targets for understanding acute bone loss under post-fracture unloading conditions.

Availability of Data and Materials

The data used to support the findings of this study are available from the corresponding author upon request.

Author Contributions

BCW conducted the main experiments, analyzed the data, and drafted the manuscript. XBW, as the corresponding author, conceived and supervised the study, interpreted the results, and revised the manuscript. ZRW and MJB contributed to parts of the experimental work and data organization. All authors revised it critically for important intellectual content, approved the final manuscript, and agreed to be accountable for all aspects of the work.

Ethics Approval and Consent to Participate

This study adheres to The ARRIVE guidelines 2.0 regarding animal ethics. The study protocol was reviewed and approved by the Institutional Animal Care and Use Committee of Beijing Jishuitan Hospital, Capital Medical University (approval No. [2025-02-05]).

Acknowledgment

Not applicable.

Funding

This work was supported by the Public Welfare Development and Reform Pilot Program of Beijing Municipal Medical Research Institutions (Grant No. JYY2023-11).

Conflict of Interest

The authors declare no conflict of interest.

References

[1] Ren P, Sun W, Wang D, Zhang Y, Tian Z, Ma G, *et al*. Sustained release PLGA microspheres loaded with a bone-affinity Bmp2 enhance fracture healing and mitigate heterotopic ossification. Bioactive Materials. 2026; 61: 796–814. https://doi.org/10.1016/j.bioactmat.2026.02.050.

[2] Claes L, Recknagel S, Ignatius A. Fracture healing under healthy and inflammatory conditions. Nature Reviews. Rheumatology. 2012; 8: 133–143. https://doi.org/10.1038/nrrheum.2012.1.

[3] Bliuc D, Tran T, Adachi JD, Atkins GJ, Berger C, van den Bergh J, *et al*. Cognitive decline is associated with an accelerated rate of bone loss and increased fracture risk in women: a prospective study from the Canadian Multicentre Osteoporosis Study. Journal of Bone and Mineral Research: the Official Journal of the American Society for Bone and Mineral Research. 2021; 36: 2106–2115. https://doi.org/10.1002/jbmr.4402.

[4] Stegen S, Carmeliet G. Metabolic regulation of skeletal cell fate and function. Nature Reviews. Endocrinology. 2024; 20: 399–413. https://doi.org/10.1038/s41574-024-00969-x.

[5] Schulte FA, Marques FC, Griesbach JK, Weigt C, von Salis-Soglio M, Lambers FM, *et al*. Combined physical and pharmacological anabolic osteoporosis therapies increase bone response and mechanoregulation in female mice. Nature Communications. 2026; 17: 3759. https://doi.org/10.1038/s41467-026-70309-2.

[6] Xu M, Li Z, Thottappillil N, Cherief M, Zhu M, Xing X, *et al*. Mapping somatosensory afferent circuitry to bone identifies neurotrophic signals required for fracture healing. Science (New York, N.Y.). 2026; 391: eadr9608. https://doi.org/10.1126/science.adr9608.

[7] Dolan CP, Imholt F, Yang TJ, Bokhari R, Gregory J, Yan M, *et al*. Mouse Digit Tip Regeneration Is Mechanical Load Dependent. Journal of Bone and Mineral Research: the Official Journal of the American Society for Bone and Mineral Research. 2022; 37: 312–322. https://doi.org/10.1002/jbmr.4470.

[8] Valle-Tenney R, Peredo N, De Samblancx K, Nefyodova E, Cardoen R, Dehaemers T, *et al*. Pharmacological HIF activation protects against diet-induced obesity, glucose intolerance, and skeletal dysfunction by exerting dual beneficial effects on energy metabolism and bone. Bone Research. 2026; 14: 21. https://doi.org/10.1038/s41413-025-00503-3.

[9] Morey-Holton ER, Globus RK. Hindlimb unloading rodent model: technical aspects. Journal of Applied Physiology (Bethesda, Md.: 1985). 2002; 92: 1367–1377. https://doi.org/10.1152/japplphysiol.00969.2001.

[10] Belay T, Aviles H, Vance M, Fountain K, Sonnenfeld G. Effects of the hindlimb-unloading model of spaceflight conditions on resistance of mice to infection with Klebsiella pneumoniae. The Journal of Allergy and Clinical Immunology. 2002; 110: 262–268. https://doi.org/10.1067/mai.2002.126459.

[11] Hidaka S, Gustilo RB. Refracture of bones of the forearm after plate removal. The Journal of Bone and Joint Surgery. American Volume. 1984; 66: 1241–1243.

[12] Chen KH, Wong PC, Rethi L, Wang WR, Chen CY, Tsai PH, *et al*. Bioabsorbable magnesium-based bulk metallic glass composite (BMGC) for improved medial opening wedge high tibial osteotomy in knee osteoarthritis. Journal of Orthopaedic Translation. 2025; 50: 97–110. https://doi.org/10.1016/j.jot.2024.10.001.

[13] Qian D, Zhang Q, He CX, Guo J, Huang XT, Zhao J, *et al*. Hai-Honghua medicinal liquor is a reliable remedy for fracture by promotion of osteogenic differentiation via activation of PI3K/Akt pathway. Journal of Ethnopharmacology. 2024; 330: 118234. https://doi.org/10.1016/j.jep.2024.118234.

[14] Chen J, Wu D, Huang C, Yan Z, Wang J, Li S, *et al*. Piezo1-driven mechanotransduction regulates mitochondrial biogenesis by AMPK/SIRT1-mediated PGC-1α deacetylation to ameliorate bone loss in disuse osteoporosis. International Journal of Biological Sciences. 2026; 22: 308–326. https://doi.org/10.7150/ijbs.124043.

[15] Rah B, Shafarin J, Qaisar R, Karim A, Hamad M, Muhammad JS. Mouse hindlimb unloading, as a model of simulated microgravity, leads to dysregulated iron homeostasis in liver and skeletal muscle cells. Life Sciences in Space Research. 2025; 45: 7–15. https://doi.org/10.1016/j.lssr.2025.01.003.

[16] Allen MR, Hogan HA, Bloomfield SA. Differential bone and muscle recovery following hindlimb unloading in skeletally mature male rats. Journal of Musculoskeletal & Neuronal Interactions. 2006; 6: 217–225.

[17] Otto K, von Thaden AK. Chapter 5.4 - Anaesthesia, Analgesia and Euthanasia. In Hedrich HJ (ed.) The Laboratory Mouse (pp. 739–759). 2nd edn. Academic Press: The Laboratory Mouse (Second Edition). 2012. https://doi.org/10.1016/B978-0-12-382008-2.00032-5.

[18] Davidge A, Bulat F, Vernet A. Evaluating cervical dislocation methods, without using tension on the tail, for humanely killing adult laboratory mice. Laboratory Animals. 2025; 59: 570–577. https://doi.org/10.1177/00236772251332722.

[19] Compston JE, McClung MR, Leslie WD. Osteoporosis. Lancet (London, England). 2019; 393: 364–376. https://doi.org/10.1016/S0140-6736(18)32112-3.

[20] Wang J, Wang Y, Zeng Y, Huang D. Feature selection approaches identify potential plasma metabolites in postmenopausal osteoporosis patients. Metabolomics: Official Journal of the Metabolomic Society. 2022; 18: 86. https://doi.org/10.1007/s11306-022-01937-0.

[21] Liu X, Yan Z, Cai J, Wang D, Yang Y, Ding Y, *et al*. Glucose- and glutamine-dependent bioenergetics sensitize bone mechanoresponse after unloading by modulating osteocyte calcium dynamics. The Journal of Clinical Investigation. 2023; 133: e164508. https://doi.org/10.1172/JCI164508.

[22] Thévenot EA, Roux A, Xu Y, Ezan E, Junot C. Analysis of the Human Adult Urinary Metabolome Variations with Age, Body Mass Index, and Gender by Implementing a Comprehensive Workflow for Univariate and OPLS Statistical Analyses. Journal of Proteome Research. 2015; 14: 3322–3335. https://doi.org/10.1021/acs.jproteome.5b00354.

[23] Westerhuis JA, van Velzen EJJ, Hoefsloot HCJ, Smilde AK. Multivariate paired data analysis: multilevel PLSDA versus OPLSDA. Metabolomics: Official Journal of the Metabolomic Society. 2010; 6: 119–128. https://doi.org/10.1007/s11306-009-0185-z.

[24] Xia J, Wishart DS. MetPA: a web-based metabolomics tool for pathway analysis and visualization. Bioinformatics (Oxford, England). 2010; 26: 2342–2344. https://doi.org/10.1093/bioinformatics/btq418.

[25] Altermann E, Klaenhammer TR. PathwayVoyager: pathway mapping using the Kyoto Encyclopedia of Genes and Genomes (KEGG) database. BMC Genomics. 2005; 6: 60. https://doi.org/10.1186/1471-2164-6-60.

[26] Kanehisa M, Goto S. KEGG: kyoto encyclopedia of genes and genomes. Nucleic Acids Research. 2000; 28: 27–30. https://doi.org/10.1093/nar/28.1.27.

[27] Xia J, Sinelnikov IV, Han B, Wishart DS. MetaboAnalyst 3.0–making metabolomics more meaningful. Nucleic Acids Research. 2015; 43: W251–W257. https://doi.org/10.1093/nar/gkv380.

[28] Kumar L, E Futschik M. Mfuzz: a software package for soft clustering of microarray data. Bioinformation. 2007; 2: 5–7. https://doi.org/10.6026/97320630002005.

[29] Conway JR, Lex A, Gehlenborg N. UpSetR: an R package for the visualization of intersecting sets and their properties. Bioinformatics (Oxford, England). 2017; 33: 2938–2940. https://doi.org/10.1093/bioinformatics/btx364.

[30] Meas SJ, Daire GM, Friedman MA, DeNapoli R, Ghosh P, Farr JN, *et al*. A comparison of bone microarchitectural and transcriptomic changes in murine long bones in response to hindlimb unloading and aging. Bone. 2024; 179: 116973. https://doi.org/10.1016/j.bone.2023.116973.

[31] Wang H, Zhao Y, Liu H, Zhang X, Lv S, Zhou T, *et al*. Untargeted metabolomics revealed the mechanism of aucubin on glucocorticoid-induced osteoporosis in mice through modulating arachidonic acid metabolism. Journal of Pharmaceutical and Biomedical Analysis. 2024; 248: 116273. https://doi.org/10.1016/j.jpba.2024.116273.

[32] Kuroyanagi G, Hioki T, Matsushima-Nishiwaki R, Omura T, Kozawa O, Tokuda H. Gallein increases prostaglandin F2α-induced osteoprotegerin and IL-6 secretion in osteoblasts. Biomedical Reports. 2024; 21: 147. https://doi.org/10.3892/br.2024.1835.

[33] Chen J, Long F. mTOR signaling in skeletal development and disease. Bone Research. 2018; 6: 1. https://doi.org/10.1038/s41413-017-0004-5.

[34] Liang Z, Su Z, Yang H, Zheng J, Wu X, Huang M, *et al*. Branched-chain amino acids in bone health: From molecular mechanisms to therapeutic potential. Biomedicine & Pharmacotherapy. 2025; 192: 118645. https://doi.org/10.1016/j.biopha.2025.118645.

[35] Lal S, Gunji S, Ahluwalia P, Kolhe R, Bollag WB, Hill WD, *et al*. Lipid metabolism in age-related musculoskeletal disorders: insights into sarcopenia and osteoporosis. BMC Biology. 2025; 23: 265. https://doi.org/10.1186/s12915-025-02383-9.

[36] Kang JH, Ko HM, Han GD, Lee SY, Moon JS, Kim MS, *et al*. Dual role of phosphatidylserine and its receptors in osteoclastogenesis. Cell Death & Disease. 2020; 11: 497. https://doi.org/10.1038/s41419-020-2712-9.

[37] Field JT, Gordon JW. BNIP3 and Nix: Atypical regulators of cell fate. Biochimica et Biophysica Acta. Molecular Cell Research. 2022; 1869: 119325. https://doi.org/10.1016/j.bbamcr.2022.119325.

[38] Lecka-Czernik B, Rosen CJ, Napoli N. The role of bone in whole-body energy metabolism. Nature Reviews. Endocrinology. 2025; 21: 743–756. https://doi.org/10.1038/s41574-025-01162-4.